PHYSICAL REVIEW D **79,** 083004 (2009)

Relativistic images of Schwarzschild black hole lensing

K. S. Virbhadra*

Department of Mathematics, Physics and Statistics, University of the Sciences in Philadelphia, Philadelphia, Pennsylvania 19104, USA

(Received 12 October 2008; published 9 April 2009)

We model massive dark objects at centers of many galaxies as Schwarzschild black hole lenses and study gravitational lensing by them in detail. We show that the ratio of mass of a Schwarzschild lens to the differential time delay between outermost two relativistic images (both of them either on the primary or on the secondary image side) is extremely insensitive to changes in the angular source position as well as the lens-source and lens-observer distances. Therefore, this ratio can be used to obtain very accurate values for masses of black holes at centers of galaxies. Similarly, angular separations between any two relativistic images are also extremely insensitive to changes in the angular source position and the lens-source distance. Therefore, with the known value of mass of a black hole, angular separation between two relativistic images would give a very accurate result for the distance of the black hole. Accuracies in determination of masses and distances of black holes would however depend on accuracies in measurements of differential time delays and angular separations between images. Deflection angles of primary and secondary images as well as effective deflection angles of relativistic images on the secondary image side are always positive. However, the effective deflection angles of relativistic images on the primary image side may be positive, zero, or negative depending on the value of angular source position and the ratio of mass of the lens to its distance. We show that effective deflection angles of relativistic images play significant role in analyzing and understanding strong gravitational field lensing.

DOI: 10.1103/PhysRevD.79.083004 PACS numbers: 98.62.Sb, 04.20.Dw, 04.70.Bw

I. INTRODUCTION

Light deflection in weak gravitational field of Schwarzschild spacetime is well-known since 1919 [1,2], and it serves as the starting point to the learning of gravitational lensing (GL) theory even now [3–5]. However, light deflection in a strong gravitational field of Schwarzschild spacetime was not studied until around 5 decades ago Darwin [6] pioneered a theoretical research on GL resulting from large deflection of light in the vicinity of photon sphere of Schwarzschild spacetime. A few years later, Atkinson [7] extended these studies to a general static spherically symmetric spacetime. In fact, apart from a few activities, the subject of strong gravitational field lensing remained in almost a dormant stage until toward the end of the last century, and this was due to two main reasons. First, Darwin's calculations showed that the images are very demagnified and therefore those are very difficult to be observed with the available observational facilities. Second, the known gravitational lens equation (see in [3,4]) was not adequate for the study of lensing due to large deflection of light. As astronomical techniques are improving fast, it may be possible to overcome the observational obstacles in the future. Therefore, an adequate lens equation was required for this purpose. To this end, Frittelli and Newman [8] obtained an exact lens equation that is applicable to arbitrary spacetimes; however, this equation is difficult to use in general. Further, under some physically realistic assumptions, we [9] obtained a simple lens equation that allows arbitrary small as well as large light deflection angles. Later, Frittelli *et al.* and Kling *et al.* [10] carried out comprehensive comparative studies of the exact lens equation with our lens equation for the case of Schwarzschild spacetime. They found that our lens equation works remarkably well as both approaches to gravitational lensing yield extremely close results even for light rays which have large deflections in strong gravitational field and go around the lens several times before reaching the observer. As our lens equation is easy to use and yields very close results to those obtained by using an exact lens equation, our lens equation has been most widely used in the literature for studying strong field gravitational lensing. Perlick [11], in a recent brief review, called our lens equation an *almost exact lens equation*. In the last 8 years, there has been a growing interest in studying weak as well as strong field lensing by black holes, naked singularities, wormholes, and some other exotic objects (see [12–24] and references therein).

In [9], we modeled the massive dark object (MDO) at the galactic center as a Schwarzschild black hole lens, and, using our lens equation, studied point source GL due to light deflections in weak as well as strong gravitational fields. By solving the lens equation numerically, we obtained image positions and their magnifications. Like in Darwin's paper, our computations showed that, in addition to primary (also called direct) and secondary images, there are theoretically an infinite sequence of very demagnified images on both sides of the optical axis; we named them

*shwetket@yahoo.com

relativistic images. With increase in the value of angular source position (measured with respect to the optical axis), magnifications of relativistic images decrease with much faster rates compared to magnifications of primary and secondary images. Therefore, relativistic images are not just very demagnified, but are also transient. However, despite several other observational difficulties (discussed in [9] and also in the last section of this paper), if these images were ever observed, we showed that it would give an upper bound to the compactness of the MDO. Therefore, it would push black hole interpretation of the MDO at the galactic center. Observation of relativistic images would be undoubtedly a landmark discovery in astronomy; however, experimentalists and astronomers have to pay the price for these very important observations. When the source, the lens, and the observer are aligned, in addition to an Einstein ring, we get theoretically an infinite sequence of rings; we [9] termed them *relativistic Einstein rings*.

The central thread in this paper is a comprehensive study of relativistic images of Schwarzschild black hole lensing. The purpose of this is to theoretically investigate if possible observations of these images, compared to primary and secondary images, could provide more valuable and accurate information about the lens. Though the primary and secondary images of Schwarzschild black hole lensing are well discussed in the literature, we also include these in this paper for 3 reasons. First, we do not take either weak or strong field approximations in our computations. Thus, our results are more accurate than known weak field limit approximate analytical expressions could provide for lensing observables for these images. Therefore, these more accurate results could be useful for observations in near future with advancing astronomical facilities. Second, it is useful to have thorough studies of relativistic as well as primary and secondary images due to a gravitational lens (with the same mass and distance) in the same paper so that one can immediately compare properties of these images. For observations of relativistic images and measurements associated with them, a detailed information about their primary and secondary images are helpful. Third, differential time delay of secondary image with respect to the primary image is though well discussed in the literature, studies of their individual time delays were not paid enough attention for some reasons (discussed later in this paper). Therefore, we study these and obtain some important results.

This paper is organized as follows. In Sec. II, we first discuss a lens equation applicable to weak as well as strong gravitational field regions, and then give a brief review of deflection angles and time delays of light rays traveling in Schwarzschild spacetime. In Sec. III, we show that a schematic diagram for effective deflection angles of relativistic images give deep insight and provide some important information before computations. In Sec. IV, we model our Galactic MDO as the Schwarzschild black hole lens and study variations in image positions, magnifications, and time delays of primary and secondary as well as relativistic images with changes in angular source position and lens to source distance. We also study the variation of deflection angles for primary and secondary images and effective deflection angles of relativistic images with respect to changes in the angular source position and lens to source distance. Computations of effective deflection angles provide geometrical beauty of strong gravitational field lensing and an analysis of those support the reasonableness of other results obtained through numerical computations. In Sec. V, we model MDOs at centers of many galaxies as Schwarzschild black hole lenses and study the variations in the same physical quantities (as studied in Sec. VI) with respect to changes in the ratio of mass of lens to its distance and the lens-source distance for a fixed value of angular source position. In Sec. VI, we discuss and summarize the results.

Bozza *et al.* [17] obtained approximate analytical expressions for image positions and magnifications of relativistic images. Bozza and Mancini [18] further derived approximate analytical expressions for differential time delays among relativistic images. As the aim of our paper is to present accurate results and to derive some important astrophysical implications for those, we do not digress to compare and contrast our results with approximate analytical results given in [17,18]. In Sec. IV, we briefly discuss that there are small (but significant) percentage differences in results for image positions. However, percentage differences in results for magnifications of images are very large. In Sec. V, we compare their approximate results with ours for differential time delays between two relativistic images. We show that there are qualitative as well as large quantitative differences. We justify our results with some arguments.

There are some fascinating results in this paper. The most important among those is that relativistic images would provide very accurate values for masses and distances of MDOs at centers of galaxies. The ratio of the mass of a Schwarzschild lens to the differential time delays between two outermost relativistic images (both of them either on the primary image side or on the secondary image side from the optical axis) is almost a constant; i.e., this ratio is *extremely* insensitive to changes in the angular source position, the observer-lens distance, and the lens-source distance. Therefore, observation of relativistic images and measurements of their differential time delays would give very accurate values for masses of MDOs. Another very useful property of relativistic images is that variations in their angular separations due to changes in the angular source position and the lens-source distance are extremely small. Therefore, once we have accurate values for masses of MDOs, measurements of angular separations between relativistic images would give very accurate re-

sults for distances of those MDOs. Similarly, we also show that the measurement of ratio of fluxes of outermost relativistic images (one on each side of the optical axis) would help us obtain very accurate result for distance of the source.

As in our previous papers on GL [9,19–21], we use geometrized units (i.e., the gravitational constant $G = 1$ and the speed of light in vacuum $c = 1$, so that $M \equiv MG/c^2$) throughout this paper. However, we finally present time delays and differential time delays of images in the unit of *minute*.

II. LENS EQUATION, DEFLECTION ANGLE, AND TIME DELAY

Assuming that the angular position of source of light is small and the source as well as the observer are situated at large distances from the lens (deflector), we [9] obtained a new gravitational lens equation that allows for arbitrary large as well as small deflections of light. The lens equation is given by

$$\tan\beta = \tan\theta - \mathcal{D}[\tan\theta + \tan(\hat{\alpha} - \theta)], \tag{1}$$

with

$$\mathcal{D} = \frac{D_{ds}}{D_s}. \tag{2}$$

Angular positions of an unlensed source and images are measured from the optical axis (the line joining the observer and the center of mass of the gravitational lens), and are represented by symbols β and θ, respectively. These angles when measured in clockwise and anticlockwise directions from the optical axis are assigned positive and negative signs, respectively. $\hat{\alpha}$ represents the total angle by which the light ray is deflected in the gravitational field of the lens while traveling from the source to the observer. Null geodesics which are bent toward and away from the lens have, respectively, $\hat{\alpha} > 0$ and $\hat{\alpha} < 0$. D_d, D_{ds}, and D_s stand, respectively, for observer-lens, lens-source, and observer-source angular diameter distances. The values of parameter $\mathcal{D}$ mathematically lie in the interval (0, 1); however, for the lens equation to hold good, the value of $\mathcal{D}$ should not be taken too close to 0. The perpendicular distance from the center of mass of the lens to the tangent to the null geodesic at the source position is (see Fig. 1 in [9])

$$J = D_d \sin\theta \tag{3}$$

and is called impact parameter.

The magnification of an image formed due to GL is defined as the ratio of the flux of the image to the flux of the unlensed source. However, according to Liouville's theorem, the surface brightness is preserved in GL. Therefore, the magnification μ of an image formed due to gravitational lensing turns out to be the ratio of the solid angles of the image and of the unlensed source made at the observer [3–5]. Thus, for a circularly symmetric GL, the magnification μ of an image is obviously expressed by

$$\mu = \mu_t \mu_r, \tag{4}$$

where the tangential magnification μ_t and the radial magnification μ_r are, respectively, expressed by

$$\mu_t = \left(\frac{\sin\beta}{\sin\theta}\right)^{-1} \quad \text{and} \quad \mu_r = \left(\frac{d\beta}{d\theta}\right)^{-1}. \tag{5}$$

Tangential critical curves (TCCs) and *radial critical curves* (RCCs) are, respectively, given by singularities in μ_t and μ_r in the lens plane. However, their corresponding values in the source plane are, respectively, termed *tangential caustic* (TC) and *radial caustics* (RCs). The parity of an image is called positive if $\mu > 0$ and negative if $\mu < 0$. Sometimes terms magnifications and absolute magnifications of negative parity images are used synonymously. If the angular source position $\beta = 0$ (i.e., when the source, the lens, and the observer are aligned), there may be ring shaped image(s) [called Einstein ring(s)]; these images are assigned 0-parity. Note that $\beta = 0$ does not always give Einstein ring(s) (for examples, see in [19–21]).

In this paper, we thoroughly study gravitational lensing due to Schwarzschild black holes, which exterior gravitational field is described by the line element

$$ds^2 = \left(1 - \frac{2M}{r}\right)dt^2 - \left(1 - \frac{2M}{r}\right)^{-1}dr^2 - r^2\left(d\vartheta^2 + \sin^2\vartheta d\phi^2\right), \tag{6}$$

where the real constant parameter M is the ADM mass. The radii of event horizon and photon sphere of a Schwarzschild black hole are given by $R_{\rm eh} = 2M$ and $R_{\rm ps} = 3M$, respectively. $R_{\rm eh}$ is also called the Schwarzschild radius.

The bending angle $\hat{\alpha}$ for a light ray with the closest distance of approach r_o is given by

$$\hat{\alpha}(r_o) = 2\int_{r_o}^{\infty} \frac{dr}{r\sqrt{(\frac{r}{r_o})^2(1 - \frac{2M}{r_o}) - (1 - \frac{2M}{r})}} - \pi \tag{7}$$

and the impact parameter J of the light ray is expressed by

$$J(r_o) = r_o\left(1 - \frac{2M}{r_o}\right)^{-1/2}. \tag{8}$$

(See in [25].) Defining a dimensionless radial distance ρ in terms of the Schwarzschild radius $2M$ by equation

$$\rho = \frac{r}{2M} \tag{9}$$

(for $r = r_o$, $\rho = \rho_o$), we [9,19] expressed the deflection angle $\hat{\alpha}(\rho)$ and the impact parameter $J(\rho)$, respectively, by

$$\hat{\alpha}(\rho_o) = 2\int_{\rho_o}^{\infty} \frac{d\rho}{\rho\sqrt{(\frac{\rho}{\rho_o})^2(1 - \frac{1}{\rho_o}) - (1 - \frac{1}{\rho})}} - \pi \tag{10}$$

and

$$J(\rho_o) = 2M\rho_o\left(1-\frac{1}{\rho_o}\right)^{-1/2}. \tag{11}$$

For computations of magnifications of images, the first derivative of deflection angle $\hat{\alpha}$ with respect to θ is needed, which is given by [9,19]

$$\frac{d\hat{\alpha}}{d\theta} = \hat{\alpha}'(\rho_o)\frac{d\rho_o}{d\theta}, \tag{12}$$

where the first and second factors on right side of this equation are, respectively, given by

$$\hat{\alpha}'(\rho_o) = \frac{3-2\rho_o}{\rho_o^2(1-\frac{1}{\rho_o})} \times \int_{\rho_o}^{\infty} \frac{(4\rho-3)d\rho}{(3-2\rho)^2\rho\sqrt{(\frac{\rho}{\rho_o})^2(1-\frac{1}{\rho_o})-(1-\frac{1}{\rho})}} \tag{13}$$

and

$$\frac{d\rho_o}{d\theta} = \frac{\rho_o(1-\frac{1}{\rho_o})^{3/2}\sqrt{1-(\frac{2M}{D_d})^2\rho_o^2(1-\frac{1}{\rho_o})^{-1}}}{\frac{M}{D_d}(2\rho_o-3)}. \tag{14}$$

Time delays for images of gravitational lensing are given by 3 terms: the first and second terms with positive sign are, respectively, the travel time of the light from the source to the point of closest approach and from that point to the observer, and the third term with a minus sign is the light travel time from the source to the observer in the absence of any gravitational field. Solving null geodesic equations for general static spherically symmetric spacetime, Weinberg in his classic book [25] obtained the time required for light to travel from a source at coordinates $\{r, \vartheta, \pi/2, \varphi = \varphi_1\}$ to the closest point of approach (to the lens) at coordinates $\{r_0, \vartheta, \pi/2, \varphi = \varphi_2\}$. Using this result, time delay of images of Schwarzschild lensing can be expressed as (see Eqs. (23)–(25) in [21])

$$\tau(\rho_0) = 2M\left[\int_{\rho_0}^{\mathcal{X}_s}\frac{d\rho}{f(\rho)} + \int_{\rho_0}^{\mathcal{X}_o}\frac{d\rho}{f(\rho)}\right] - D_s\sec\beta \tag{15}$$

with

$$\mathcal{X}_s = \frac{D_s}{2M}\sqrt{\left(\frac{D_{ds}}{D_s}\right)^2+\tan^2\beta}, \qquad \mathcal{X}_o = \frac{D_d}{2M}, \tag{16}$$

and

$$f(\rho) = \sqrt{\left(1-\frac{1}{\rho}\right)^2 - \left(\frac{\rho_0}{\rho}\right)^2\left(1-\frac{1}{\rho}\right)^3\left(1-\frac{1}{\rho_0}\right)^{-1}}. \tag{17}$$

Time delay of a gravitationally lensed image may be in general positive, zero, or negative; for examples, see in our paper [21]. However, time delays are always positive for images of Schwarzschild lensing.

It is worth mentioning that Eq. (4.67) in a classic book on GL by Schneider *et al.* [3] gives time delays of gravitationally lensed images. That equation contains an additive constant term. The authors clarified that the constant term is the same for all rays from the source plane to the observer. Therefore, this term cancels for computations of differential time delay between 2 images. However, as the value for the constant term is not obtained, that equation cannot be used to compute time delays of images. We are interested to first compute time delays of images and then use those to obtain differential time delays. This is why we use the method given in Weinberg's book [25] and we discussed that in this section.

III. EFFECTIVE DEFLECTION ANGLES OF RELATIVISTIC IMAGES

It is important to first discuss in brief a few new terms we defined in our previous paper [9]. Then, we will show that these definitions with some arguments reveal geometrical beauty of strong field Schwarzschild lensing. This also helps predict some results without computations and thus provides consistency check for results obtained through numerical computations.

If a lens is very compact, then a light ray passing close to it will suffer a large deflection and therefore will loop around the lens once, twice, thrice, or many times (depending on the closest distance of approach from the center of the lens) before reaching the observer. We [9] defined *relativistic images* of GL as those images which occur due to light deflections by angles $\hat{\alpha} > 3\pi/2$. Similarly, for the angular source position $\beta = 0$, we defined *relativistic Einstein rings* as those ringed-shaped images which can form due to light deflections by angles $\hat{\alpha} > 2\pi$. Relativistic Einstein rings are thus relativistic images for the case of $\beta = 0$. It is useful to define *order* of relativistic images on each side of the optical axis. We assign the order 1 to the outermost relativistic images on both sides of the optical axis, 2 for adjacent inner ones, and so on. Thus, according to this definition, the outermost relativistic Einstein ring also has the order 1.

In a recent paper [21], we discussed that the existence of a photon sphere enclosing a lens is a sufficient (not necessary) condition for the formation of relativistic images. A sufficiently compact lens can give rise to relativistic images even if the lens is not covered inside a photon sphere. Therefore, the lens need not be a black hole to produce these images.

In [9], we defined a term *effective deflection angle* of a relativistic image, which we now express as follows:

$$\hat{\alpha}^e(\rho_0) = \hat{\alpha}(\rho_0) - 2n\pi, \tag{18}$$

where n is a positive integer that represents the number of loops (turns) a light ray makes around the lens before reaching the observer, and the superscript e on $\hat{\alpha}$ stands for the word *effective*. (In fact, the above equation can also

be applied to primary and secondary images, because $n = 0$ correspond to those images. However, we prefer to call those as known in the literature instead of calling them images of 0-order.) $\hat{\alpha}(\rho_0)$, as given by Eq. (10), is the usual (total) deflection angle for the light ray with the closest scaled distance of approach ρ_0 making n loops around the lens. Thus, similar to the cases of primary and secondary images, the effective deflection angle of a relativistic image turns out to be the angle between the tangents on the null geodesic at the source and at the observer positions. In the following, we now introduce new symbols we use for physical quantities associated with primary, secondary, and relativistic images.

New symbols.—We use subscripts p and s, respectively, for primary and secondary images. Similarly, subscripts np and ns ($n = 1, 2, 3, \ldots$) stand, respectively, for the images of order n on the same side as the primary and secondary images. For example, $\hat{\alpha}^e_{1p}$ and $\hat{\alpha}^e_{1s}$, respectively, stand for effective deflection angles of relativistic images of order 1 on the same side as the primary and secondary images. The same applies to symbols for angular image positions, magnifications, and time delays.

It is well-known that, on the same side as the source from the optical axis, the Schwarzschild black hole lensing gives rise to the primary image which is formed due to light deflection in weak gravitational field without looping of the ray of light around the lens. On the other hand, relativistic images on the same side as the source are produced due to looping of light rays around the lens, which is caused by large deflection angles $\hat{\alpha} > 3\pi/2$ in strong gravitational field. It is natural to ask if, excluding the primary image, there is any other image (on the same side as the source from the optical axis) which can form without looping of the light ray around the black hole. Computations give no such solutions to the lens equation. Therefore, on the same side as the source, there is only one (i.e., the primary) image which forms due to light deflection in weak field without looping of the light ray around the lens and there are relativistic images which arise due to looping of light rays around the lens in strong gravitational field. In the following, we will show that a simple geometrical argument beautifully supports these numerical results.

See Fig. 1. Assume that, on the same side as the source from the optical axis, two light rays emitted from the source S reach the observer O without looping around

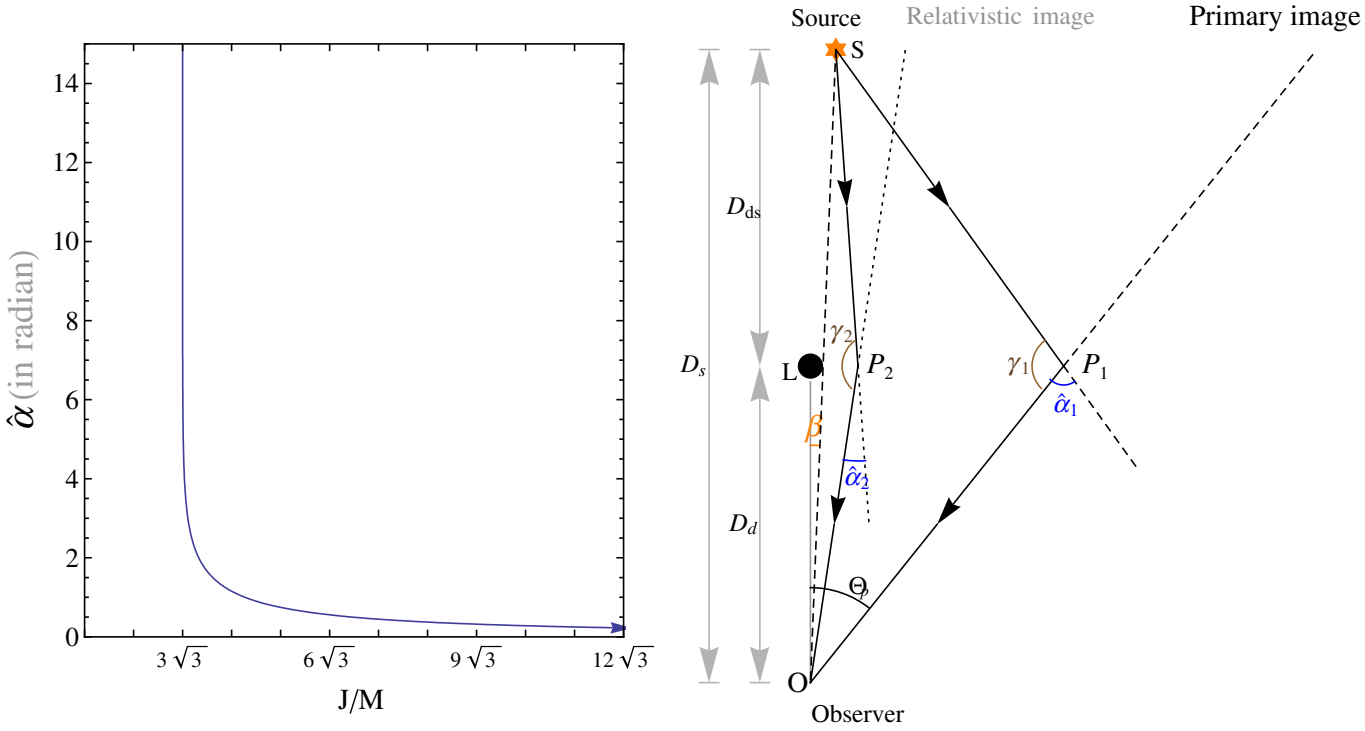

FIG. 1 (color online). *Left*: The deflection angle $\hat{\alpha}$ is plotted against the dimensionless scaled impact parameter J/M. The arrow attached to the curve indicates that $\hat{\alpha}$ decreases with increase in the value of J/M. *Right*: S, L, and O represent positions of the source, the lens, and the observer, respectively. SP_1 and SP_2 are tangents on 2 null geodesics at the source position, whereas P_1O and P_2O are tangents on, respectively, the same pair of null geodesics at the observer position. $\hat{\alpha}_1$ and $\hat{\alpha}_2$ are light bending angles, whereas γ_1 and γ_2 are their respective supplementary angles. β and θp stand, respectively, for the angular positions of the source and the primary image. Angles in this schematic diagram are greatly exaggerated. $\gamma_2 > \gamma_1 \Rightarrow \hat{\alpha}_2 < \hat{\alpha}_1$. According to the $\hat{\alpha}$ vs J/M plot (on left side), $\hat{\alpha}_2 < \hat{\alpha}_1$ is possible only if SP_2 and P_2O are, respectively, tangents at the source and the observer positions on a null geodesic which loops around the lens at least once giving rise to a relativistic image.

the lens. SP_1 and SP_2 are tangents on 2 null geodesics at the source position, and, similarly, P_1O and P_2O are, respectively, tangents on those null geodesics at the observer position. $\hat{\alpha}_1$ and $\hat{\alpha}_2$ are deflections angles corresponding to 2 light rays we considered and γ_1 and γ_2 are their respective supplementary angles. The schematic diagram (right of Fig. 1) shows that $\gamma_2 > \gamma_1$. This implies that $\hat{\alpha}_2 < \hat{\alpha}_1$, which is not allowed according to the $\hat{\alpha}$ vs J/M graph (see the left of Fig. 1); i.e., a decrease in the impact parameter should increase $\hat{\alpha}$. Thus if the light path SP_1O is allowed, then SP_2O is not allowed and therefore we conclude that there can be only the primary image on the same side as the source without the light ray looping around the lens. A similar argument also demonstrates that there can be only one image (i.e., secondary) on the opposite side from the source without a light ray going around the lens.

Now consider that SP_2 and P_2O represent tangents, respectively, at the source and the observer position on a null geodesic that loops around the lens once before reaching the observer. Therefore, $\hat{\alpha}_2 = \hat{\alpha}^e_{1p} < \hat{\alpha}_1$, which also reflects in numerical computations in next section. For a given value of β, the schematic diagram also shows that the effective deflection angle of relativistic images on the same side as the primary image decrease with increase in its order. Similarly, for a given angular source position, the effective deflection angles of relativistic images (on the same side as the secondary) decreases with the increase in its order. These conclusions based on simple geometrical analysis are reflected in results of our numerical computations in the next section.

In Fig. 2, we show that effective deflection angles of relativistic images on the same side as the primary image can be positive, zero, or negative depending on the value of the angular source position. However, for relativistic images on the same side as the secondary image, effective deflection angles are always positive. Consider the first order relativistic images on both side of the optical axis; i.e., one on the primary image side and the other on the secondary image side. SC_1 and C_1O are, respectively, tangents on null geodesics (giving rise to the 1st order relativistic image on the primary image side) at the source and observer positions; C_1 is their point of intersection. Similarly, SC_2 and C_2O are, respectively, tangents on null geodesics (giving rise to the 1^{st} order relativistic image on the secondary image side) at the source and observer positions; C_2 is their point of intersection. As the angular source position β increases, the intersection points C_1 and

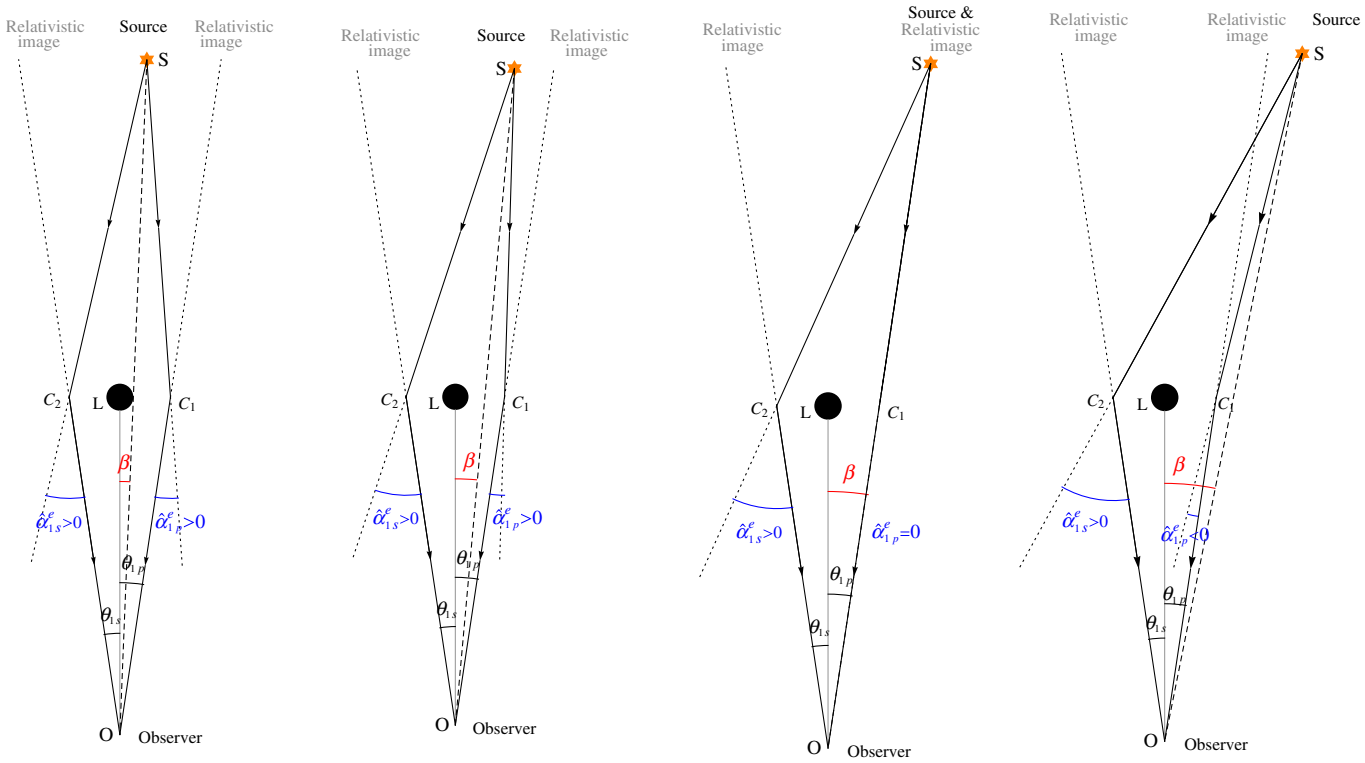

FIG. 2 (color online). Schematic diagram showing the variation in effective deflection angles of relativistic images with respect to increase in the value of angular source position β. S, L, and O stand for the position of the source, the lens, and the observer, respectively. SC_1 and SC_2 are tangents on 2 null geodesics at S, and C_1O and C_2O are tangents on corresponding null geodesics at O. $\hat{\alpha}^e_{1p}$ and $\hat{\alpha}^e_{1s}$ stand for effective deflection angles of relativistic images of order 1, respectively, on the primary and secondary image sides; θ_{1p} and θ_{1s} are their respective angular image positions. Angles are greatly exaggerated.

C_2 move extremely slowly, respectively, away from and toward the lens. For small angular source position β, the effective deflection angle $\hat{\alpha}^e_{1p} > 0$ (see the extreme left diagram). As the value of β increases, the value of $\hat{\alpha}^e_{1p}$ decreases to zero value (see the second and third diagrams from the left). When $\hat{\alpha}^e_{1p} = 0$, the angular source position of this relativistic image and the source coincide. We denote this critical value of the angular source position as β_{1c}. (Subscript c stands for the word *critical* and 1 stands for the 1st order relativistic image.) A further increase in the value of β makes the effective deflection angle $\hat{\alpha}^e_{1p} < 0$ and its value keep decreasing with increase in the value of β. On the other hand, the effective deflection angles of relativistic images on the same side as the secondary image increases with the increase in the value of β. These important conclusions based on simple geometrical analysis also appear in our numerical results in the next section. Therefore, the geometrical analysis using Figs. 1 and 2 also supports correctness of our computations.

IV. GRAVITATIONAL LENSING BY THE GALACTIC MDO

In this section, we model the MDO at the center of our Galaxy (the Milky Way) as a Schwarzschild black hole lens and study point source GL in a great detail. The MDO has the mass $M = 3.61 \times 10^6 M_\odot$ and is at the distance $D_d = 7.62$ kpc from us [26]. Therefore, $M/D_d \approx 2.26 \times 10^{-11}$ (note that $M \equiv MG/c^2$). In a recent paper [21], we already obtained angular positions, deflection angles, magnifications, and time delays for primary and secondary images for several values of angular source position β for $\mathcal{D} \equiv D_{ds}/D_s = 0.5$ (i.e., when the lens is situated halfway between the observer and the source). We also computed differential time delays of secondary images with respect to primary images. For comparison and continuity in discussion, we use those results in this paper and also put those in Table I. Now considering $\mathcal{D} = 0.5$ and using *Mathematica*, we numerically solve the gravitational lens Eq. (1) for a large number of values for β and obtain image positions for first and second order relativistic images on both sides of the optical axis. We further obtain deflection angles, magnifications, time delays, and differential time delays for these images. Using Eq. (18), we obtain effective deflection angles for these relativistic images. We put these results in Tables II and III. Though we computed for a large number of values for β, we put only a few data in tables; however, we use all those for figures. We further repeat the entire computations for primary and secondary as well as relativistic images for $\mathcal{D} = 0.05$ and 0.005 to see the effects of changes in image positions, deflection/effective deflection angles, magnifications, time delays, and differential time delays due to change in the lens-source distance. (With the observer-lens distance D_d fixed, a decrease in the value of $\mathcal{D}$ decreases the source-lens distance D_{ds}.) Throughout our computations in this paper, we never take either weak or strong gravitational field approximation and therefore our computations and hence results are *exact* in this sense. In the following paragraphs, we will now discuss results for GL by the Galactic MDO.

In Fig. 3, we first plot the (absolute) angular positions (measured from the optical axis) of primary and secondary images, and their separations against the angular source position β for $\mathcal{D} = 0.5$, 0.05 and 0.005. As it is well-known that, for a given value of $\mathcal{D}$, the angular positions

TABLE I. Angular positions, bending angles, magnifications, and time delays of primary and secondary images due to GL by the Galactic MDO modeled as a Schwarzschild black hole. β stands for the angular source position. θ, $\hat{\alpha}$, μ, and τ stand, respectively, for angular positions, deflection angles, magnifications, and time delays of images, with p and s subscripts, respectively, for primary and secondary images. $\tau_s - \tau_p$ stands for the differential time delay of the secondary image with respect to the primary image. All angles are expressed in *arcsec*, and time delays and differential time delays are given in *minutes*. (a) The Galactic MDO (lens) has mass $M = 3.61 \times 10^6 M_\odot$, which is at distance $D_d = 7.62$ kpc. $M/D_d \approx 2.26 \times 10^{-11}$, where $M \equiv MG/c^2$. The ratio of the lens-source distance to the observer-source distance $\mathcal{D} = 0.5$. Results in this table are taken from our recent paper [21].

β	Secondary image					Primary image			
	θ_s	$\hat{\alpha}_s$	μ_s	τ_s	$\tau_s - \tau_p$	θ_p	$\hat{\alpha}_p$	μ_p	τ_p
0	−1.388176	2.776352	×	14.9220910	0	1.388176	2.776352	×	14.9220910
10^{-6}	−1.388176	2.776353	−694084.2	14.9220919	0.000002	1.388177	2.776351	694085.2	14.9220902
10^{-5}	−1.388171	2.776362	−69407.97	14.9220995	0.000017	1.388181	2.776342	69408.97	14.9220825
10^{-4}	−1.388126	2.776452	−6940.347	14.9221763	0.000171	1.388226	2.776252	6941.347	14.9220057
10^{-3}	−1.387676	2.777353	−693.5848	14.9229442	0.001706	1.388676	2.775353	694.5848	14.9212382
10^{-2}	−1.383185	2.786370	−68.90982	14.9306363	0.017060	1.393185	2.766370	69.90982	14.9135764
10^{-1}	−1.339077	2.878153	−6.454348	15.0089452	0.170636	1.439076	2.678152	7.454345	14.8383092
1	−0.975480	3.950960	−0.322455	15.9468061	1.742193	1.975475	1.950951	1.322453	14.2046135
2	−0.710863	5.421726	−0.073840	17.3803344	3.687537	2.710855	1.421709	1.073838	13.6927977
3	−0.543786	7.087573	−0.024114	19.2981794	5.987040	3.543776	1.087553	1.024113	13.3111391
4	−0.434559	8.869117	−0.009696	21.7471848	8.734391	4.434547	0.869094	1.009695	13.0127934
5	−0.359561	10.71912	−0.004521	24.7549479	11.98479	5.359549	0.719098	1.004521	12.7701628

TABLE II. Effective deflection angles, magnifications, and time delays of relativistic images (on the same side as the primary image) due to GL by the Galactic MDO modeled as a Schwarzschild black hole. $\hat{\alpha}^e$, μ, and τ stand, respectively, for effective deflection angles, magnifications, and time delays, with $1p$ and $2p$ subscripts, respectively, are used for the first and the second order relativistic images on the same side as the primary image. $\tau_{2p} - \tau_{1p}$, $\tau_{1p} - \tau_p$, and $\tau_{1p} - \tau_s$ are differential time delays. The angular positions of the first and second order relativistic images on the primary image side are, respectively, $\theta_{1p} \approx 24.30283$ μas and $\theta_{2p} \approx 24.27240$ μas for all values of angular source position β considered in this table. (a) The angular source positions and the effective deflection angles are, respectively, expressed in *arcsec* and μas, whereas time delays and differential time delays are given in *minutes*. The mass and distance of the lens are as given in (a) of Table I.

β	Second order (inner) relativistic image				First order (outer) relativistic image				
	$\hat{\alpha}^e_{2p}$	μ_{2p}	τ_{2p}	$\tau_{2p} - \tau_{1p}$	$\hat{\alpha}^e_{1p}$	μ_{1p}	τ_{1p}	$\tau_{1p} - \tau_p$	$\tau_{1p} - \tau_s$
0	48.544793	$\times$	48.0274920	9.666638229	48.605666	$\times$	38.3608537	23.438763	23.438763
10^{-6}	46.544793	1.34×10^{-14}	48.0274920	9.666638229	46.605666	7.21×10^{-12}	38.3608537	23.438764	23.438762
10^{-5}	28.544793	1.34×10^{-15}	48.0274920	9.666638229	28.605666	7.21×10^{-13}	38.3608537	23.438771	23.438754
10^{-4}	-151.45521	1.34×10^{-16}	48.0274920	9.666638229	-151.39433	7.21×10^{-14}	38.3608537	23.438848	23.438677
10^{-3}	-1951.4552	1.34×10^{-17}	48.0274922	9.666638229	-1951.3943	7.21×10^{-15}	38.3608540	23.439616	23.437910
10^{-2}	-19951.455	1.34×10^{-18}	48.0275225	9.666638229	-19951.394	7.21×10^{-16}	38.3608843	23.447308	23.430248
10^{-1}	-199951.46	1.34×10^{-19}	48.0305628	9.666638231	-199951.39	7.21×10^{-17}	38.3639246	23.525615	23.354979
1	-1999951.5	1.34×10^{-20}	48.3347132	9.666638248	-1999951.4	7.21×10^{-18}	38.6680749	24.463461	22.721269

of primary and secondary images, respectively, increase and decrease with an increase in the value of β. For a given value of β, the angular positions of primary as well as secondary images increase with an increase in the value of $\mathcal{D}$. The angular radius of Einstein ring increases with increase in the value of $\mathcal{D}$. The angular separation between primary and secondary images increases with increase in β and $\mathcal{D}$. The angular positions of relativistic images are very insensitive to changes in the values of β and $\mathcal{D}$. The angular position of the first order relativistic images on both sides of the optical axis have extremely close values; however, $\theta_{1p} > |\theta_{1s}|$ for all values of β, excluding, of course, at $\beta = 0$ for which $\theta_{1p} = |\theta_{1s}|$. The same is true for any pair of second or higher order relativistic images. As θ_{np} and $|\theta_{ns}|$ (for the same value of n) have extremely close values, we plot image positions of relativistic images only on the same side as the primary image. For theoretical interest, it is worth investigating variation in the value of θ_{np} and $|\theta_{ns}|$ with changes in the value of β and $\mathcal{D}$, though variations are extremely small. For relativistic images of a given order n and for a given value of $\mathcal{D}$, the values in θ_{np} and $|\theta_{ns}|$, respectively, increase and decrease with the increase in the value of β, though the increase and decrease are extremely small. However, their dependence on $\mathcal{D}$ is much more fascinating. For $\beta = 0$ or a small value, θ_{1p} is greater for a greater value of $\mathcal{D}$. As β increases, there is situation when θ_{1p} is the same for all values of $\mathcal{D}$. At this critical angular source position $\beta_{1c} \approx 24.3028$ *microarcsec* (μas), the effective deflection angle $\hat{\alpha}^e_{1p} = 0$ for all values of $\mathcal{D}$. For a further increase in the value of β, θ_{1p} is smaller for a greater value of $\mathcal{D}$. The same happens for any relativistic images on the same side as the primary image; however, critical angular source position β_{nc} decreases with an increase in the order n of the image; for example, $\beta_{2c} \approx 24.2724$ μas. On the other hand, for any fixed value of β, image positions of relativistic images (on the sec-

TABLE III. Effective deflection angles, magnifications, and time delays of relativistic images (on the same side as the secondary image) due to GL by the Galactic MDO modeled as a Schwarzschild black hole. $\hat{\alpha}^e$, μ, and τ stand, respectively, for effective deflection angles, magnifications, and time delays, with subscripts $1s$ and $2s$, respectively, are used for the first and the second order relativistic images on the secondary image side. $\tau_{1s} - \tau_{1p}$, $\tau_{1s} - \tau_p$, $\tau_{1s} - \tau_s$, and $\tau_{2s} - \tau_{1p}$ are differential time delays. The angular positions of the first and second order relativistic images on the secondary image side are, respectively, $\theta_{1s} \approx -24.30283$ μas and $\theta_{2s} \approx -24.27240$ μas for all values of angular source position β considered in this table. (a) The same as (a) of Table II.

β	First (outer) relativistic image						Second (inner) relativistic image			
	$\hat{\alpha}^e_{1s}$	μ_{1s}	τ_{1s}	$\tau_{1s} - \tau_{1p}$	$\tau_{1s} - \tau_p$	$\tau_{1s} - \tau_s$	$\hat{\alpha}^e_{2s}$	μ_{2s}	τ_{2s}	$\tau_{2s} - \tau_{1p}$
0	48.605666	$\times$	38.3608537	0	23.438763	23.438763	48.544793	$\times$	48.0274920	9.666638229
10^{-6}	50.605666	-7.21×10^{-12}	38.3608537	2.99×10^{-11}	23.438764	23.438762	50.544793	-1.34×10^{-14}	48.0274920	9.666638229
10^{-5}	68.605666	-7.21×10^{-13}	38.3608537	2.99×10^{-10}	23.438771	23.438754	68.544793	-1.34×10^{-15}	48.0274920	9.666638230
10^{-4}	248.60567	-7.21×10^{-14}	38.3608537	2.99×10^{-9}	23.438848	23.438677	248.54479	-1.34×10^{-16}	48.0274920	9.666638232
10^{-3}	2048.6057	-7.21×10^{-15}	38.3608540	2.99×10^{-8}	23.439616	23.437910	2048.5448	-1.34×10^{-17}	48.0274923	9.666638259
10^{-2}	20048.606	-7.21×10^{-16}	38.3608846	2.99×10^{-7}	23.447308	23.430248	20048.545	-1.34×10^{-18}	48.0275228	9.666638528
10^{-1}	200048.61	-7.21×10^{-17}	38.3639276	2.99×10^{-6}	23.525618	23.354982	200048.54	-1.34×10^{-19}	48.0305658	9.666641214
1	2000048.6	-7.21×10^{-18}	38.6681048	2.99×10^{-5}	24.463491	22.721299	2000048.5	-1.34×10^{-20}	48.3347430	9.666668077

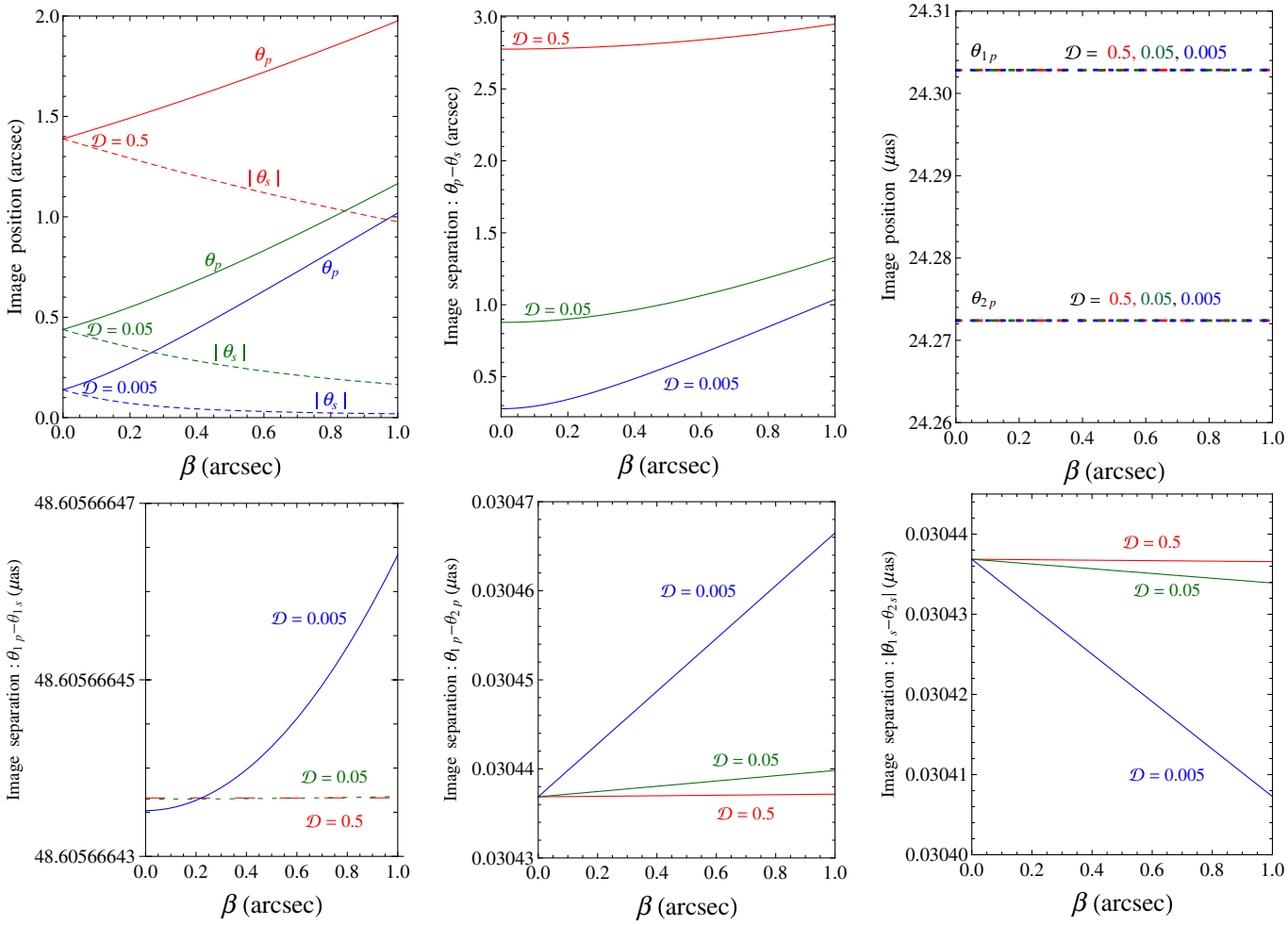

FIG. 3 (color online). *Top left and middle*: The angular positions of primary images θ_p, secondary images $|\theta_s|$, and their separations $\theta_p - \theta_s$ are plotted against the angular source position β for $\mathcal{D} = 0.5$, 0.05 and 0.005. *Top right*: The angular positions of relativistic images (on the same side as the primary image) of the first order θ_{1p} and of the second order θ_{2p} are plotted against β for the same values of $\mathcal{D}$ as in the figures on left. The curves for θ_{1p} (for different values of $\mathcal{D}$) intersect for $\beta_{1c} \approx 24.3028$ μas, whereas those for θ_{2p} intersect for $\beta_{2c} \approx 24.2724$ μas. *Below*: The angular separations among relativistic images versus the angular source position β are plotted for $\mathcal{D} = 0.5$, 0.05 and 0.005. θ_{np} and θ_{ns} ($n = 1, 2$) stand for angular positions of relativistic images on the primary and the secondary image sides, respectively. The Galactic MDO is modeled as the Schwarzschild lens, which has mass $M = 3.61 \times 10^6 M_\odot$ and is situated at the distance $D_d = 7.62$ kpc so that $M/D_d \approx 2.26 \times 10^{-11}$.

ondary image side) $|\theta_{ns}|$ always increase with an increase in $\mathcal{D}$. The angular separation between relativistic images of the first order (i.e, $\theta_{1p} - \theta_{1s}$) increases with an increase in the value of β (for a fixed $\mathcal{D}$). The increase rate of the angular separation with increase in β is higher for lower value of $\mathcal{D}$. For $\beta = 0$ or a small value, this angular separation is higher for a higher value of $\mathcal{D}$. (This is qualitatively similar to the case of image separation between primary and secondary images.) However, for large value of β, the angular separation $\theta_{1p} - \theta_{1s}$ is higher for lower value of $\mathcal{D}$. For any two values of $\mathcal{D}$, there exist a β at which values of $\theta_{1p} - \theta_{1s}$ are equal for both $\mathcal{D}$. The angular separations between outermost 2 relativistic images (both of them either on the primary or on the secondary image side) have just opposite qualitative dependence on β and $\mathcal{D}$ in the following sense. $\theta_{1p} - \theta_{2p}$ increases with increase in β (for a fixed $\mathcal{D}$), but decreases with increase in $\mathcal{D}$ (for a fixed β). On the other hand, $|\theta_{1s} - \theta_{2s}|$ decreases with increase in β (for a fixed $\mathcal{D}$), but increases with increase in $\mathcal{D}$ (for a fixed β). The increase/decrease rate with change in the value of β (for a fixed $\mathcal{D}$) is smaller for higher value of $\mathcal{D}$. The variations in angular separations between relativistic images are very small with respect to changes in β and $\mathcal{D}$. Among angular separations $\theta_{1p} - \theta_{1s}$, $\theta_{1p} - \theta_{2p}$, and $|\theta_{1s} - \theta_{2s}|$, the first one is the least sensitive to those changes. As relativistic images would be observationally important for very small values of β, we conclude that angular separations between relativistic images of our interest are extremely insensitive to change in the value of $\mathcal{D}$.

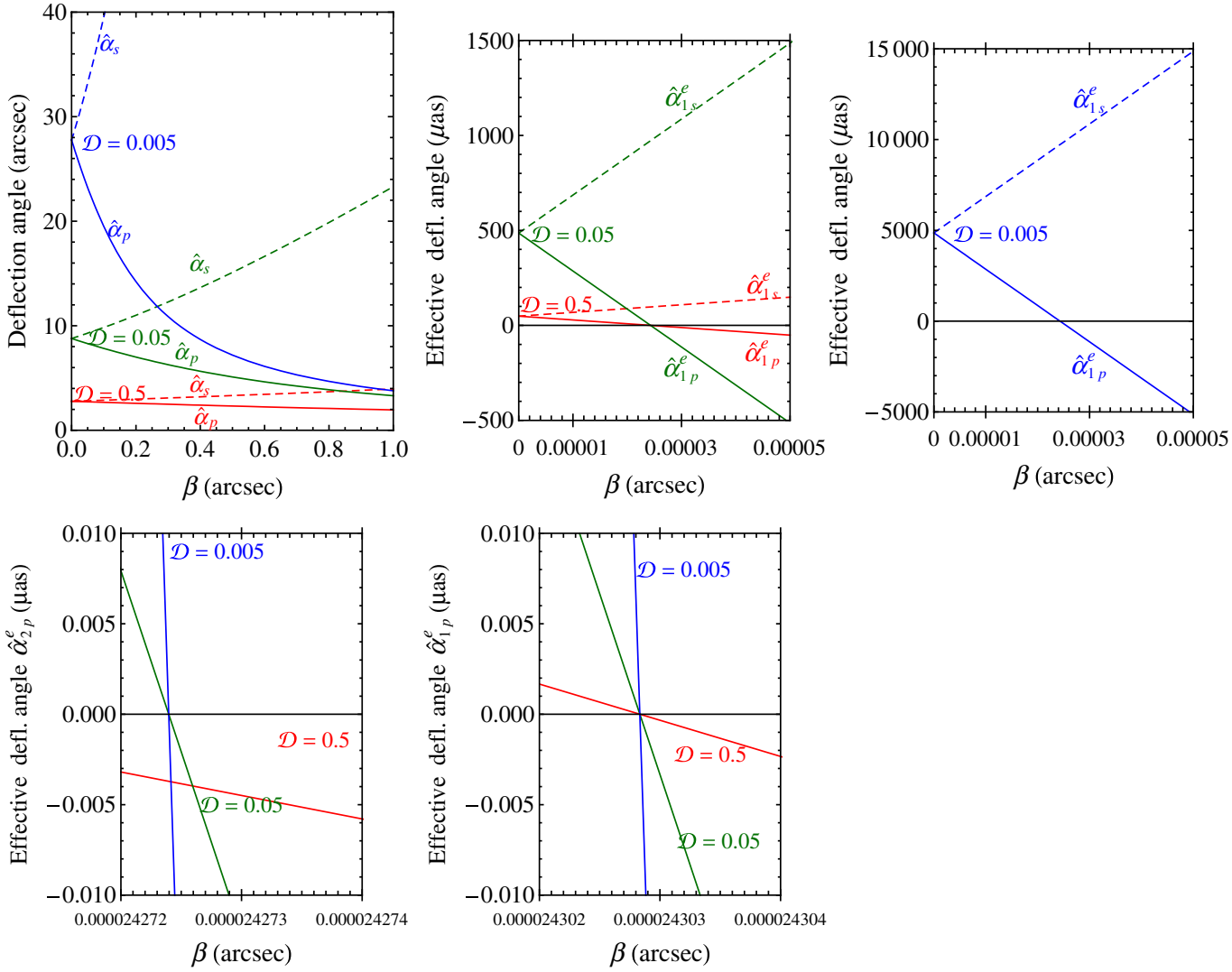

FIG. 4 (color online). *Top left*: The deflection angles of primary images $\hat{\alpha}_p$ and secondary images $\hat{\alpha}_s$ are plotted against the angular source position β for $\mathcal{D} = 0.5$, 0.05 and 0.005. *Top middle and right*: The effective deflection angles of the first order relativistic images on the same side as the primary image $\hat{\alpha}^e_{1p}$ and on the same side as the secondary image $\hat{\alpha}^e_{1s}$ are plotted against β for $\mathcal{D} = 0.5$, 0.05 and 0.005. *Below left and right*: The effective deflection angles of the second order $\hat{\alpha}^e_{2p}$ (left) and of the first order $\hat{\alpha}^e_{1p}$ (right), both on the same side as the primary image, are plotted against β for $\mathcal{D} = 0.5$, 0.05 and 0.005 in the vicinity of zero effective deflection angle. $\beta_{2c} \approx 24.2724$ μas and $\beta_{1c} \approx 24.3028$ μas, where β_{2c} and β_{1c} are, respectively, critical angular source positions for the second and first order relativistic images. The gravitational lens is the same as for the Fig. 3.

In Fig. 4, we show variations in deflection angles for primary and secondary as well as effective deflection angles for relativistic images with respect to changes in values for β and $\mathcal{D}$. It is known that for a given value of $\mathcal{D}$, the deflection angles for primary and secondary images, respectively, decrease and increase with an increase in the value of β. For a fixed value of β, deflection angles for these images increase with decrease in the value of $\mathcal{D}$. Like primary and secondary images, the deflection angles of relativistic images are always positive, and the same is true for effective deflection angles of relativistic images on the secondary image side. However, for a fixed value of M/D_d, the effective deflection angles of relativistic images on the same side as the primary image decrease with an increase in the value of β, and can be positive, zero, or negative depending on the value of β. For a relativistic image (of any order) on the same side as the primary image, there exists a critical value of β for which the effective deflection angle is zero. These results are as expected from the schematic diagram in Fig. 2. Our numerical computations give $\beta_{2c} \approx 24.2724$ μas and $\beta_{1c} \approx 24.3028$ μas showing that $\beta_{2c} < \beta_{1c}$. The effective deflection angle is positive, zero, and negative, respectively, for the angular source position less than, equal to, and greater than the critical value of the angular source position. The critical source positions are independent of the value of $\mathcal{D}$. As expected from the schematic diagram (see Fig. 2), our computations also show that effective deflec-

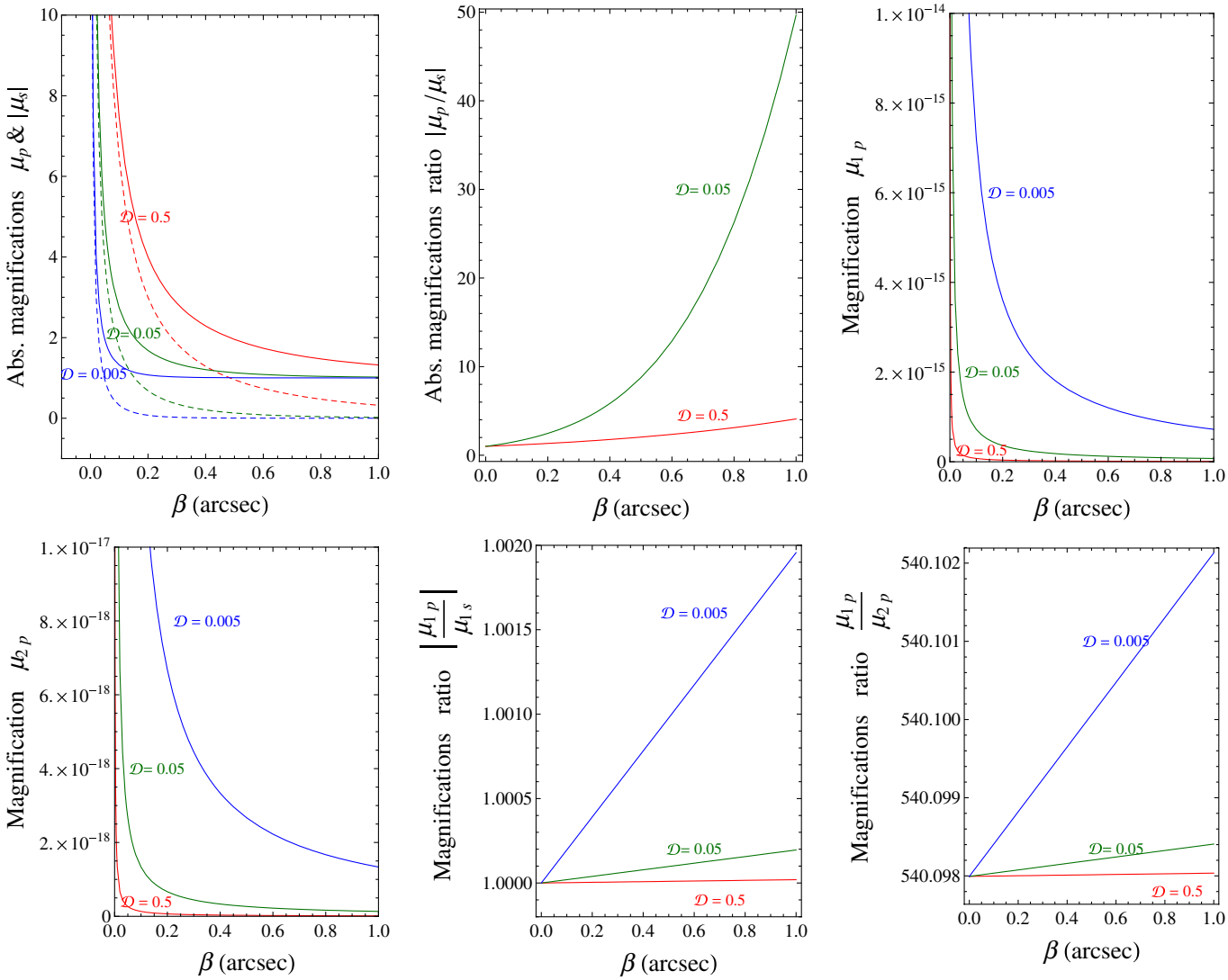

FIG. 5 (color online). *Top left and middle*: The magnifications of primary images μ_p, the absolute magnifications of secondary images $|\mu_s|$, and their ratios $|\mu_p/\mu_s|$ are plotted against the angular source position β for different values of $\mathcal{D}$. *Top right and below left*: The magnifications of relativistic images (on the same side as the primary image) of the first order μ_{1p} and the second order μ_{2p} are plotted against the angular source position β for $\mathcal{D} = 0.5$, 0.05 and 0.005. *Below middle and right*: The magnifications ratios $|\mu_{1p}/\mu_{1s}|$ (where μ_{1s} stands for magnification of the first order relativistic image on the same side as the secondary image) and μ_{1p}/μ_{2p} vs β are plotted for the same values of $\mathcal{D}$ as in the figure on below left. The lens is the same as for the Fig. 3.

tion angles of relativistic images on the secondary image side are always positive and increase with increase in the value of β (for fixed $\mathcal{D}$).

In Fig. 5, we show changes in (absolute) magnifications of primary and secondary images as well as relativistic images with changes in the values of β and $\mathcal{D}$. Images on the same side as the source and opposite side from the source have, respectively, positive and negative magnifications and therefore have, respectively, positive and negative parities. The (absolute) magnifications of primary, secondary, and relativistic images decrease with an increase in the value of angular source position β. However, there are 2 important differences between absolute magnifications of primary-secondary pair and relativistic images. First, the absolute magnifications of relativistic images are extremely small and decrease much faster than those of primary and secondary images with an increase in the angular source position β. Secondly, as opposed to the case of primary and secondary images, for a fixed value of β, the absolute magnifications of relativistic images increase with decrease in the value of $\mathcal{D}$. Therefore, it would be easier to observe relativistic images of those sources which are relatively nearer to the lens. The absolute magnifications of relativistic images of the same order on each side of the optical axis have extremely close values (images on the same side as the primary image have though slightly higher value than images on the same side as the secondary image). This is

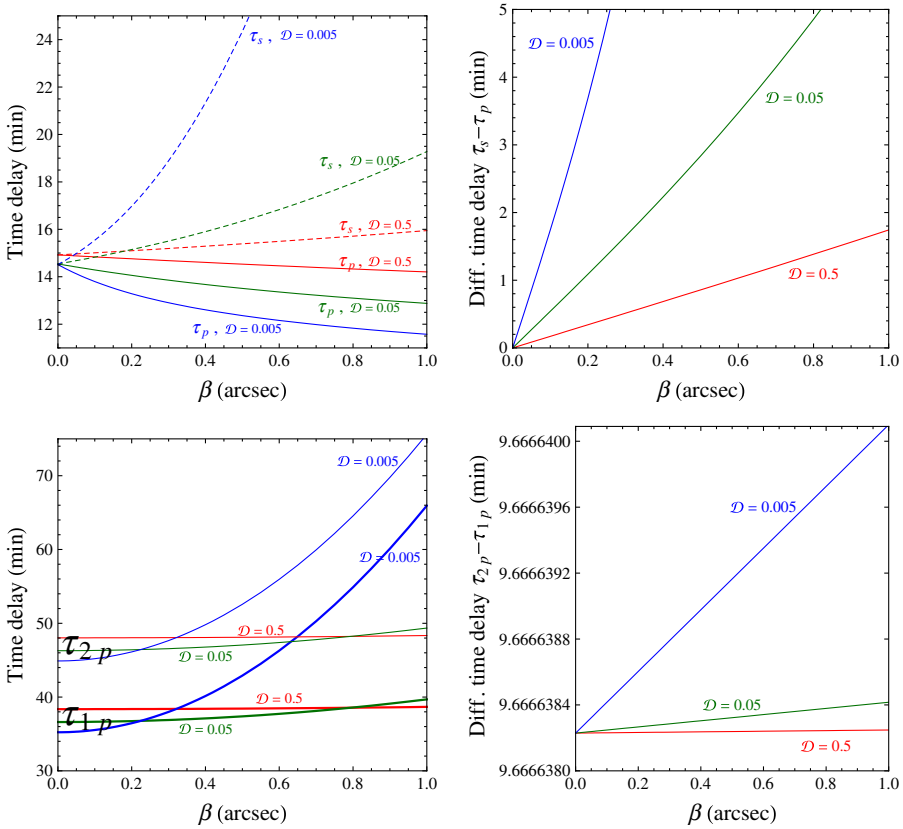

FIG. 6 (color online). *Top*: The time delays of primary images τ_p and secondary images τ_s, and the differential time delays of the secondary images with respect to their respective primary images (i.e., $\tau_s - \tau_p$) are plotted against the angular source position β for $\mathcal{D} = 0.5$, 0.05 and 0.005. *Below*: The time delays of relativistic images (on the same side as the primary image) of the first order τ_{1p}, second order τ_{2p}, and the differential time delays (i.e., $\tau_{2p} - \tau_{1p}$) are plotted against β for the same values $\mathcal{D}$ as in figures on top. The lens is the same as for the Figs. 3 through 5.

why we plot only for relativistic images on the primary image side. For a fixed value of $\mathcal{D}$, the ratios of absolute magnifications of primary and secondary images $|\mu_p/\mu_s|$, and of relativistic images $|\mu_{1p}/\mu_{1s}|$ and μ_{1p}/μ_{2p} increase with increase in the value of β. However, for a given value β, these decrease with an increase in $\mathcal{D}$. Compared to the (absolute) magnifications ratio of primary and secondary images, the ratios of (absolute) magnifications of relativistic images are much less sensitive to changes in β and $\mathcal{D}$.

In Fig. 6, we first plot time delays of primary and secondary images, and differential time delays of secondary images with respect to their respective primary images against the angular source position β for $\mathcal{D} = 0.5$, 0.05, and 0.005. For Einstein rings ($\beta = 0$ case), time delay decreases with a decrease in the value of $\mathcal{D}$. For any given value of $\mathcal{D}$, the time delays of primary and secondary images, respectively, decrease and increase with increase in the value of β. Similarly, for any given value of β, time delay of a primary image decreases with a decrease in the value of $\mathcal{D}$. However, there is no such simple dependence for the time delays of secondary images on $\mathcal{D}$. For a small value of β, time delay of secondary image is smaller for smaller $\mathcal{D}$ and the difference decreases as β increases. For a certain value of β, time delays for secondary image for 2 different values of $\mathcal{D}$ become equal. For a further increase in β, time delays for secondary images are higher for lower value of $\mathcal{D}$ and the difference keeps increasing with increase in β. For a fixed value of $\mathcal{D}$, the differential time delay of secondary image with respect to the primary image increases with increase in β. However, for a fixed value of β, this differential time delay increases with decrease in $\mathcal{D}$. We now plot time delays of relativistic images of the first and second orders (both on the same side as the primary image), and the differential time delay of the first with respect to the second against β for $\mathcal{D} = 0.5$, 0.05, and 0.005. The time delays of relativistic images of the same order on each side of the optical axis have extremely close values (images on the same side as the primary image though have lower values than images on the same side as the secondary image). This is why we plot only for relativistic images on the primary image side. The differential time delay ($\tau_{2p} - \tau_{1p}$) has simple dependence on β and $\mathcal{D}$. For a fixed value of $\mathcal{D}$, the differential time delay increases with an increase in the value of β; however, for any fixed value of β, the differential time delay increases with a decrease in the value of $\mathcal{D}$. For fixed β and

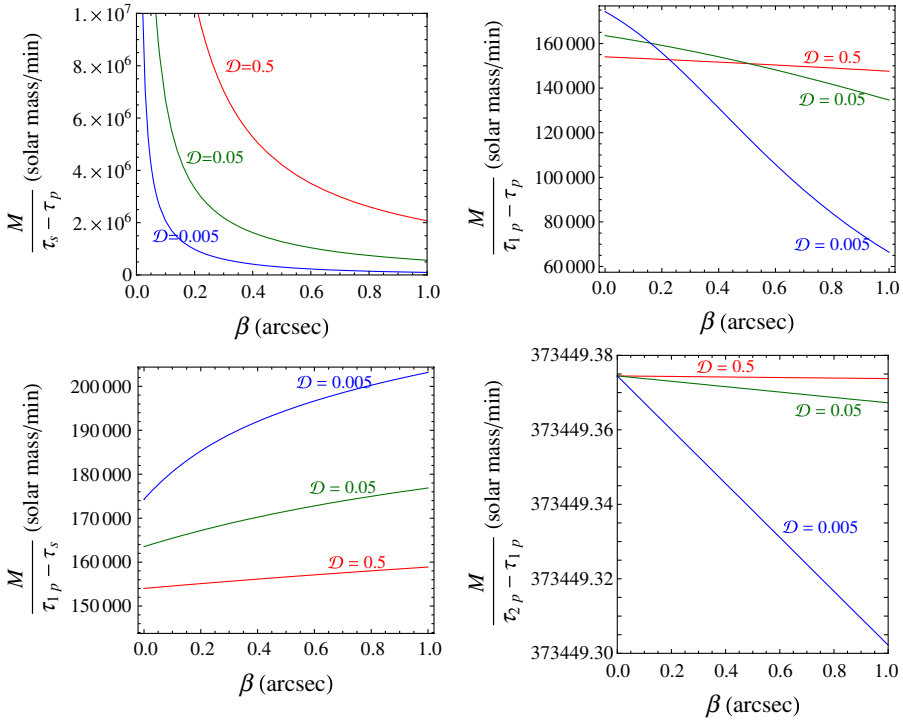

FIG. 7 (color online). The ratios of mass M of the lens to differential time delays of images are plotted against the angular source position β for $\mathcal{D} = 0.5$, 0.05 and 0.005. τ_p and τ_s stand for time delays of primary and secondary images, respectively. τ_{1p} and τ_{2p}, respectively, represent time delays of relativistic images (on the same side as the primary image) of orders 1 and 2. The gravitational lens is the same as for the Figs. 3 through 6.

$\mathcal{D}$, time delays of relativistic images increase with increase in the order; i.e., inner relativistic images have higher time delays relative to outer relativistic images. For a given value of $\mathcal{D}$ and order n, time delay of a relativistic image increases with increase in the value of β; the rate of increase is higher for lower values of $\mathcal{D}$. However, for a fixed value of β and order n of relativistic image, the dependence of time delays on $\mathcal{D}$ is not so simple. For $\beta = 0$ or a small value, the time delay of a relativistic image of a given order is smaller for a smaller value $\mathcal{D}$; however, for a certain value of β, both equal and as β increases further, time delay is higher for a lower value of $\mathcal{D}$.

In Fig. 7, we plot ratios of the mass of the lens to differential time delays among images against the angular source position β for $\mathcal{D} = 0.5$, 0.05, and 0.005. We choose 4 differential time delays: (a) differential time delay of secondary image with respect to the primary image; i.e., $\tau_s - \tau_p$, (b) differential time delay of the first order relativistic image (on the same side as the primary image) with respect to the primary image, i.e., $\tau_{1p} - \tau_p$, (c) differential time delay of the first order relativistic image (on the same side as the primary image) with respect to the secondary image, i.e., $\tau_{1p} - \tau_s$, and (d) differential time delay of the second order relativistic image with respect to the first order relativistic image (both on the same side as the primary image), i.e., $\tau_{2p} - \tau_{1p}$. We do not consider some other combinations for differential time delays for obvious reasons; for example, we do not use $\tau_{1s} - \tau_{1p}$, because these are too small (see Tables II and III) to be measured possibly in several decades to come. For a fixed value of $\mathcal{D}$, ratios $M/(\tau_s - \tau_p)$, $M/(\tau_{1p} - \tau_p)$, and the ratio $M/(\tau_{2p} - \tau_{1p})$ decrease and $M/(\tau_{1p} - \tau_s)$ increase with increase in the value of β. For any given value of β, $M/(\tau_s - \tau_p)$ and $M/(\tau_{2p} - \tau_{1p})$ decrease and $M/(\tau_{1p} - \tau_s)$ increases with a decrease in the value of $\mathcal{D}$; however, dependence of $M/(\tau_{1p} - \tau_p)$ on $\mathcal{D}$ is somewhat complex and fascinating. For $\beta = 0$ or a small value, the ratio $M/(\tau_{1p} - \tau_p)$ is higher for smaller $\mathcal{D}$. As β increases, 2 curves for 2 different values of $\mathcal{D}$ intersect and hence this ratio is the same for both values of $\mathcal{D}$. For a further increase in β, the ratio is now higher for higher value of $\mathcal{D}$. Figure 7 shows that the ratio $M/(\tau_{2p} - \tau_{1p})$ is the most insensitive to changes in values of β and $\mathcal{D}$. In fact, as the relativistic images can be observed only for $\beta = 0$ or a very small value, the variation in the ratio $M/(\tau_{2p} - \tau_{1p})$ due to change in $\mathcal{D}$ is extremely small. In the next section, we will show that this ratio is in fact extremely insensitive to change in the value of M/D_d as well. Therefore, the physical quantity $M/(\tau_{2p} - \tau_{1p})$ can be approximately considered as a constant, which can be used to compute very accurate values for masses of black holes once differential time delays $\tau_{2p} - \tau_{1p}$ are measured.

We mentioned in the first section of this paper that Bozza *et al.* [17] analytically obtained approximate expressions for image positions and magnifications of rela-

tivistic images. In order to calculate angular positions of these images, they first obtained an expression for effective deflection angles (though they did not use this term). Here, we briefly compare our results with their by giving some examples. For the purpose of comparison, we consider the MDO at the center of the Milky way as the lens. This lens has $M/D_d \approx 2.26 \times 10^{-11}$. We consider the lens to be situated halfway between the source and the observer (i.e., $\mathcal{D} = 0.5$) and the angular source position $\beta = 1$ μas. Compared to our results, Bozza *et al.* expressions give $\approx 0.5\%$ higher values for each of the following: $\hat{\alpha}^e_{1p}$ (effective deflection angle of the relativistic image of order 1 on the primary image side), θ_{1p} (angular position of the relativistic image of order 1 on the primary image side), and $\theta_{1p} - \theta_{1s}$ (angular separation between relativistic images of the first order). Though, percentage differences appear small, these are significant for 2 reasons. We have shown that the angular positions of relativistic images and their separations are extremely insensitive to changes in the angular source position as well as lens-source distance. In view of this fact, the above percentage differences are significant. In the next section, we show that angular separation between 2 relativistic images can be used to obtain very accurate value for distance of a lens. Therefore, percentage errors in Bozza *et al.* results will decrease accuracies in determination of distances of MDOs. Secondly, observation of relativistic images would provide a method to test the general theory of relativity against alternative theories of gravity in strong gravitational field region. Angular positions of relativistic images of the same order and the same parity in different theories of gravity are expected to be very close. Therefore, very accurate theoretical results for image positions would be required to compare different theories of gravity. We now compare results for magnifications of relativistic images due to the same lens. For $\mathcal{D} = 0.5$ and $\beta = 1$ μas, Bozza *et al.* result yields $\approx 372\%$ higher value than our for μ_{1p} (magnification of the first order relativistic image on the primary image side). This very large percentage difference appears to be due to unrealistic approximation they took in their calculation. Moreover, according to their result, the absolute magnification of relativistic images of the same order are equal; i.e. $|\mu_{np}/\mu_{ns}| = 1$, which is obviously not correct due to the asymmetry ($\beta \neq 0$). Our results show that $|\mu_{np}/\mu_{ns}| > 1$, as expected. For qualitative similarities between Bozza *et al.* and our results, see [17]. Bozza and Mancini [18] also analytically obtained approximate expressions for differential time delays among relativistic images. In the next section, we show that there are again large percentage errors in their results.

V. GRAVITATIONAL LENSING BY MDOS AT CENTERS OF MANY GALAXIES

In this section, we model MDOs at centers of 40 galaxies as Schwarzschild black hole lenses and, like in the previous section, study point source GL by them. Gebhardt [27] tabulated updated values of masses and distances of many

TABLE IV. Masses and distances of MDOs at centers of 40 galaxies are presented in the decreasing order of dimensionless ratio of mass to distance [i.e., $M/D_d \equiv MG/(c^2 D_d)$] of MDOs. The mass and distance of the Galactic MDO and all other MDOs are, respectively, taken from [26,27].

MDO in galaxy	Mass M in $M_\odot$	Distance D_d in Mpc	$\frac{M}{D_d}$	MDO in galaxy	Mass M in $M_\odot$	Distance D_d in Mpc	$\frac{M}{D_d}$
Milky Way	3.61×10^6	0.00762	2.26467×10^{-11}	NGC5845	2.4×10^8	25.9	4.42959×10^{-13}
NGC4486(M87)	3.0×10^9	16.1	8.90733×10^{-12}	NGC3377	1.0×10^8	11.2	4.26810×10^{-13}
NGC4649	2.0×10^9	16.8	5.69080×10^{-12}	NGC3608	1.9×10^8	22.9	3.96616×10^{-13}
NGC4594	1.1×10^9	9.80	5.36561×10^{-12}	NGC4473	1.1×10^8	15.7	3.34923×10^{-13}
NGC3115	1.0×10^9	9.70	4.92811×10^{-12}	NGC6251	5.3×10^8	93.0	2.72424×10^{-13}
NGC224(M31)	7.0×10^7	0.760	4.40288×10^{-12}	NGC7052	3.3×10^8	58.7	2.68737×10^{-13}
IC1459	2.5×10^9	29.2	4.09270×10^{-12}	NGC2787	4.1×10^7	7.50	2.61321×10^{-13}
NGC5128(cenA)	2.4×10^8	4.20	2.73158×10^{-12}	NGC4258	3.9×10^7	7.20	2.58931×10^{-13}
NGC4374(M84)	1.0×10^9	18.4	2.59797×10^{-12}	NGC4596	7.8×10^7	16.8	2.21941×10^{-13}
NGC3998	5.6×10^8	14.1	1.89855×10^{-12}	NGC4459	7.0×10^7	16.1	2.07838×10^{-13}
NGC4486B	6.0×10^8	16.1	1.78147×10^{-12}	NGC1023	4.4×10^7	11.4	1.84502×10^{-13}
NGC4350	6.0×10^8	16.8	1.70724×10^{-12}	NGC4564	5.6×10^7	15.0	1.78463×10^{-13}
NGC4342	3.1×10^8	15.3	9.68551×10^{-13}	NGC221(M32)	2.9×10^6	0.810	1.71145×10^{-13}
NGC3031(M81)	6.8×10^7	3.90	8.33483×10^{-13}	NGC821	8.5×10^7	24.1	1.68599×10^{-13}
NGC4261	5.2×10^8	31.6	7.86627×10^{-13}	NGC3384	1.6×10^7	11.6	6.59348×10^{-14}
NGC4697	1.7×10^8	11.7	6.94569×10^{-13}	NGC1068	1.5×10^7	15.0	4.78027×10^{-14}
CygnusA	2.9×10^9	240.	5.77616×10^{-13}	NGC4742	1.4×10^7	15.5	4.31766×10^{-14}
NGC4291	3.1×10^8	26.2	5.65604×10^{-13}	NGC7332	1.5×10^7	23.0	3.11757×10^{-14}
NGC3245	2.1×10^8	20.9	4.80314×10^{-13}	NGC2778	1.4×10^7	22.9	2.92244×10^{-14}
NGC3379	1.0×10^8	10.6	4.50969×10^{-13}	NGC4945	1.4×10^6	3.70	1.80875×10^{-14}

MDOs. In Table IV, we consider most of those and arrange in the decreasing order of M/D_d (i.e., the ratio of mass M and the distance D_d) of MDOs. (Only for the Galactic MDO, we use the updated values of mass and distance given in [26].) The aim of this section is to study variations in angular positions of images and their separations, deflection angles (effective deflection angles for relativistic images), magnifications and their ratios, time delays, differential time delays, and ratios of the mass of the lens to differential time delays due to changes in the value of M/D_d for $\mathcal{D} \equiv D_{ds}/D_s = 0.5$, 0.05, and 0.005. We mentioned in the first section that the central thread in this

TABLE V. Angular positions, magnifications, and time delays of primary and secondary images due to GL by MDOs (modeled as Schwarzschild black holes) at centers of many galaxies. θ, μ, and τ stand, respectively, for angular positions, magnifications and time delays of images; subscripts p and s attached to them stand, respectively, for primary and secondary images. $\tau_s - \tau_p$ stands for the differential time delay of the secondary image with respect to the primary image. The time delays and differential time delays are given in *minutes*, whereas angular positions of images are expressed in *arcsec*. (a) The first column gives the names of galaxies having MDOs with decreasing value of the ratio of mass to the distance (i.e., M/D_d). The ratio of the lens-source distance to the observer-source distance $\mathcal{D} = 0.5$. The angular source position $\beta = 1$ μas.

MDO in galaxy	Secondary image				Primary image		
	θ_s	μ_s	τ_s	$\tau_s - \tau_p$	θ_p	μ_p	τ_p
Milky Way	−1.388176	−694084.2	14.92209	1.71×10^{-6}	1.388177	694085.2	14.92209
NGC4486(M87)	−0.870593	−435294.8	12859.74	0.00226	0.870594	435295.8	12859.74
NGC4649	−0.695869	−347933.4	8720.112	0.00189	0.695870	347934.4	8720.110
NGC4594	−0.675695	−337846.2	4806.677	0.00107	0.675696	337847.2	4806.675
NGC3115	−0.647562	−323779.8	4383.655	0.00101	0.647563	323780.8	4383.654
NGC224(M31)	−0.612081	−306039.8	308.1496	0.00008	0.612082	306040.8	308.1495
IC1459	−0.590127	−295062.6	11035.30	0.00278	0.590128	295063.6	11035.29
NGC5128(cenA)	−0.482112	−241055.1	1075.303	0.00033	0.482113	241056.1	1075.302
NGC4374(M84)	−0.470173	−235085.9	4488.653	0.00140	0.470174	235086.9	4488.652
NGC3998	−0.401930	−200964.7	2542.451	0.00091	0.401931	200965.7	2542.450
NGC4486B	−0.389340	−194669.5	2730.318	0.00101	0.389341	194670.5	2730.317
NGC4350	−0.381143	−190570.7	2734.506	0.00103	0.381144	190571.7	2734.505
NGC4342	−0.287079	−143539.0	1441.646	0.00071	0.287080	143540.0	1441.646
NGC3031(M81)	−0.266310	−133154.8	317.9070	0.00017	0.266311	133155.8	317.9068
NGC4261	−0.258716	−129357.8	2435.988	0.00132	0.258717	129358.8	2435.987
NGC4697	−0.243107	−121553.1	799.8507	0.00046	0.243108	121554.1	799.8503
CygnusA	−0.221697	−110848.0	13732.21	0.00858	0.221698	110849.0	13732.20
NGC4291	−0.219379	−109689.4	1468.994	0.00093	0.219380	109690.4	1468.993
NGC3245	−0.202163	−101081.3	1000.754	0.00068	0.202164	101082.3	1000.754
NGC3379	−0.195890	−97944.75	477.5836	0.00034	0.195891	97945.75	477.5833
NGC5845	−0.194143	−97071.07	1146.906	0.00081	0.194144	97072.07	1146.905
NGC3377	−0.190571	−95285.11	478.4866	0.00034	0.190572	95286.11	478.4862
NGC3608	−0.183707	−91852.93	911.4108	0.00068	0.183708	91853.93	911.4101
NGC4473	−0.168815	−84407.35	530.7089	0.00043	0.168816	84408.35	530.7085
NGC6251	−0.152252	−76125.46	2575.005	0.00228	0.152253	76126.46	2575.003
NGC7052	−0.151218	−75608.63	1604.042	0.00143	0.151219	75609.63	1604.041
NGC2787	−0.149117	−74558.08	199.4783	0.00018	0.149118	74559.08	199.4781
NGC4258	−0.148433	−74216.33	189.8064	0.00017	0.148434	74217.33	189.8062
NGC4596	−0.137422	−68710.93	381.5847	0.00037	0.137423	68711.93	381.5844
NGC4459	−0.132985	−66491.96	343.2016	0.00035	0.132986	66492.96	343.2012
NGC1023	−0.125296	−62647.94	216.5861	0.00023	0.125297	62648.94	216.5859
NGC4564	−0.123229	−61614.25	275.9607	0.00030	0.123230	61615.25	275.9604
NGC221(M32)	−0.120676	−60337.77	14.31073	0.00002	0.120677	60338.77	14.31072
NGC821	−0.119775	−59887.15	419.6616	0.00047	0.119776	59888.15	419.6611
NGC3384	−0.074902	−37450.84	81.45874	0.00014	0.074903	37451.84	81.45860
NGC1068	−0.063777	−31888.16	77.15868	0.00015	0.063778	31889.16	77.15853
NGC4742	−0.060612	−30305.91	72.24847	0.00015	0.060613	30306.91	72.24832
NGC7332	−0.051504	−25751.92	78.21023	0.00019	0.051505	25752.92	78.21004
NGC2778	−0.049866	−24932.96	73.14462	0.00018	0.049867	24933.96	73.14444
NGC4945	−0.039231	−19615.00	7.424624	0.00002	0.039232	19616.00	7.424600

TABLE VI. Angular positions, magnifications, and time delays of the first and second order relativistic images on the same side as the primary image. MDOs at centers of many galaxies are modeled as Schwarzschild black hole lenses. θ, μ, and τ stand, respectively, for angular positions, magnifications, and time delays of images. Subscript p stands for the primary image, whereas $1p$, and $2p$ stand, respectively, for the first and second order relativistic images on the same side as the primary image. Angular positions of the images are expressed in μas, whereas the time delays and differential time delays are given in *minutes*. Other inputs are the same as (a) of Table V.

MDO in galaxy	Second order relativistic image				First order relativistic image			
	θ_{2p}	μ_{2p}	τ_{2p}	$\tau_{2p}-\tau_{1p}$	θ_{1p}	μ_{1p}	τ_{1p}	$\tau_{1p}-\tau_{p}$
Milky Way	24.272396	1.34×10^{-14}	48.02749	9.66664	24.302833	7.21×10^{-12}	38.36085	23.43876
NGC4486(M87)	9.5467556	2.07×10^{-15}	40830.26	8033.22	9.5587269	1.12×10^{-12}	32797.05	19937.31
NGC4649	6.0993161	8.43×10^{-16}	27514.08	5355.48	6.1069644	4.55×10^{-13}	22158.61	13438.50
NGC4594	5.7507837	7.49×10^{-16}	15153.98	2945.51	5.7579950	4.05×10^{-13}	12208.46	7401.788
NGC3115	5.2818819	6.32×10^{-16}	13804.24	2677.74	5.2885053	3.41×10^{-13}	11126.50	6742.847
NGC224(M31)	4.7189445	5.05×10^{-16}	968.8844	187.442	4.7248619	2.73×10^{-13}	781.4426	473.2931
IC1459	4.3864944	4.36×10^{-16}	34662.92	6694.35	4.3919950	2.36×10^{-13}	27968.57	16933.28
NGC5128(cenA)	2.9276717	1.94×10^{-16}	3359.469	642.657	2.9313429	1.05×10^{-13}	2716.812	1641.509
NGC4374(M84)	2.7844704	1.76×10^{-16}	14014.24	2677.74	2.7879620	9.49×10^{-14}	11336.50	6847.846
NGC3998	2.0348357	9.38×10^{-17}	7905.583	1499.53	2.0373873	5.07×10^{-14}	6406.049	3863.599
NGC4486B	1.9093511	8.26×10^{-17}	8482.795	1606.64	1.9117454	4.46×10^{-14}	6876.151	4145.834
NGC4350	1.8297948	7.59×10^{-17}	8491.171	1606.64	1.8320893	4.10×10^{-14}	6884.527	4150.022
NGC4342	1.0380797	2.44×10^{-17}	4444.741	830.099	1.0393814	1.32×10^{-14}	3614.642	2172.996
NGC3031(M81)	0.8933152	1.81×10^{-17}	978.3253	182.086	0.8944354	9.77×10^{-15}	796.2390	478.3322
NGC4261	0.8430953	1.61×10^{-17}	7491.180	1392.42	0.8441526	8.70×10^{-15}	6098.755	3662.769
NGC4697	0.7444293	1.26×10^{-17}	2455.980	455.216	0.7453628	6.78×10^{-15}	2000.764	1200.914
CygnusA	0.6190806	8.69×10^{-18}	42071.51	7765.44	0.6198569	4.69×10^{-15}	34306.07	20573.87
NGC4291	0.6062068	8.33×10^{-18}	4499.436	830.099	0.6069670	4.50×10^{-15}	3669.337	2200.344
NGC3245	0.5147940	6.01×10^{-18}	3059.264	562.325	0.5154395	3.24×10^{-15}	2496.939	1496.185
NGC3379	0.4833420	5.29×10^{-18}	1458.860	267.774	0.4839481	2.86×10^{-15}	1191.086	713.5030
NGC5845	0.4747576	5.11×10^{-18}	3502.675	642.657	0.4753529	2.76×10^{-15}	2860.018	1713.113
NGC3377	0.4574487	4.74×10^{-18}	1460.666	267.774	0.4580223	2.56×10^{-15}	1192.892	714.4060
NGC3608	0.4250877	4.09×10^{-18}	2779.838	508.770	0.4256208	2.21×10^{-15}	2271.068	1359.658
NGC4473	0.3589661	2.92×10^{-18}	1615.480	294.551	0.3594163	1.58×10^{-15}	1320.929	790.2203
NGC6251	0.2919802	1.93×10^{-18}	7819.582	1419.20	0.2923463	1.04×10^{-15}	6400.381	3825.378
NGC7052	0.2880290	1.88×10^{-18}	4870.271	883.654	0.2883902	1.02×10^{-15}	3986.617	2382.577
NGC2787	0.2800806	1.78×10^{-18}	605.4707	109.787	0.2804318	9.60×10^{-16}	495.6833	296.2053
NGC4258	0.2775189	1.75×10^{-18}	576.0530	104.432	0.2778669	9.43×10^{-16}	471.6212	281.8150
NGC4596	0.2378733	1.28×10^{-18}	1156.050	208.864	0.2381716	6.93×10^{-16}	947.1863	565.6019
NGC4459	0.2227576	1.12×10^{-18}	1038.988	187.442	0.2230370	6.07×10^{-16}	851.5464	508.3452
NGC1023	0.1977463	8.86×10^{-19}	654.7971	117.821	0.1979942	4.79×10^{-16}	536.9766	320.3907
NGC4564	0.1912746	8.29×10^{-19}	833.9894	149.953	0.1915144	4.48×10^{-16}	684.0360	408.0756
NGC221(M32)	0.1834313	7.62×10^{-19}	43.22856	7.76544	0.1836613	4.12×10^{-16}	35.46312	21.15240
NGC821	0.1807017	7.40×10^{-19}	1267.462	227.608	0.1809283	4.00×10^{-16}	1039.854	620.1931
NGC3384	0.0706679	1.13×10^{-19}	243.5083	42.8438	0.0707566	6.11×10^{-17}	200.6645	119.2059
NGC1068	0.0512343	5.95×10^{-20}	229.8712	40.1661	0.0512985	3.21×10^{-17}	189.7051	112.5466
NGC4742	0.0462761	4.85×10^{-20}	215.0139	37.4883	0.0463341	2.62×10^{-17}	177.5255	105.2772
NGC7332	0.0334136	2.53×10^{-20}	231.9743	40.1661	0.0334555	1.37×10^{-17}	191.8082	113.5982
NGC2778	0.0313223	2.22×10^{-20}	216.8061	37.4883	0.0313615	1.20×10^{-17}	179.3178	106.1734
NGC4945	0.0193859	8.52×10^{-21}	21.90093	3.74883	0.0194102	4.60×10^{-18}	18.15210	10.72750

paper is the study of relativistic images and we know that these images may be observed only when the lens components (the observer, the lens, and the source) are perfectly or highly aligned. In view of this we take the angular source position $\beta = 1$ μas for computations. (As we also want to compute magnifications of images due to point source GL, we do not take $\beta = 0$.) For $\beta = 1$ μas, $\mathcal{D} =$ 0.5, and different values of M/D_d for several MDOs, we numerically solve the lens equation to obtain image positions of primary and secondary as well as relativistic images of orders 1 and 2. Further, we compute deflection angles, magnifications, time delays, and differential time delays for primary and secondary as well as relativistic images. From deflection angles of relativistic images, we

compute effective deflection angles. In Tables V and VI, we present results, respectively, for primary and secondary images, and for relativistic images. Though we do not display results for deflection angles of primary and secondary images, and effective deflection angles for relativistic images in tables, we use those in figures. Further, we repeat the entire computations for $\mathcal{D} = 0.05$ and 0.005. As in the previous section, we do not take either weak or strong gravitational field approximation in any part of our computations and therefore our results are very accurate. With all results available, we present several plots and discuss these in the following paragraphs. We do not present some results for relativistic images on the secondary image side, because computations show that those results for the same order relativistic images on both sides of the optical axis are extremely close and therefore graphs for those do not appear resolved on figure.

In Fig. 8, we first plot the angular positions of primary and secondary images, and their separations against the ratios of the mass of the lens to its distance (i.e., M/D_d) for $\mathcal{D} = 0.5$, 0.05, and 0.005. As expected from well-known analytical expressions for primary and secondary image positions, the angular positions of these images, for a given value of the angular source position β, increase with increase in the values of M/D_d and $\mathcal{D}$. As we have taken $\beta = 1$ μas (a very small value), the curves for primary and

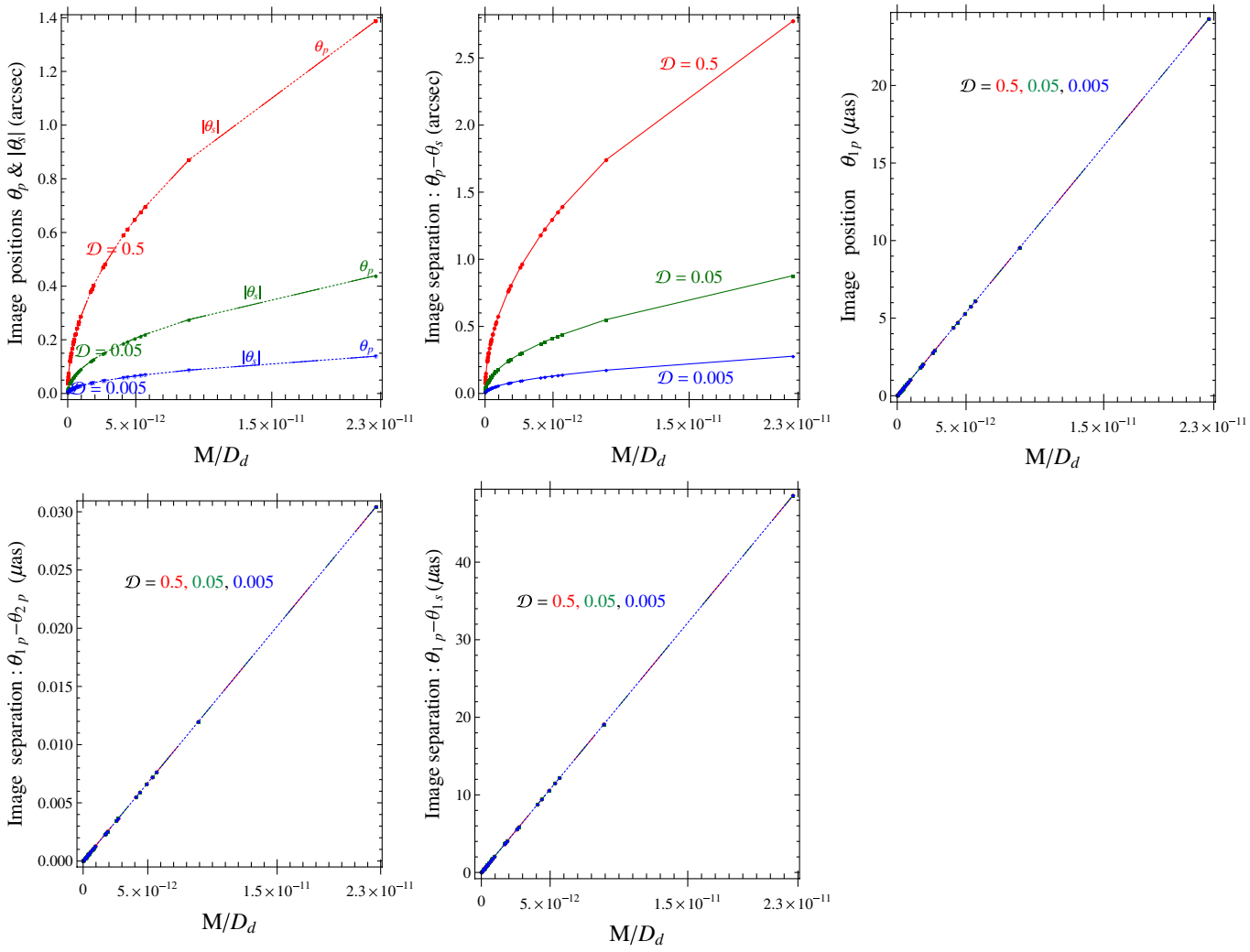

FIG. 8 (color online). *Top left and middle*: The angular positions of primary images θ_p (represented by continuous curves), secondary images $|\theta_s|$ (represented by dotted curves), and their separations $\theta_p - \theta_s$ are plotted against M/D_d of MDOs at centers of many galaxies for $\mathcal{D} = 0.5$, 0.05 and 0.005. *Top right*: The angular positions of the relativistic images (on the same side as the primary image) of the first order θ_{1p} are plotted against M/D_d for the same values of $\mathcal{D}$ as in figures on left. The curves for θ_{1p} for different values of $\mathcal{D}$ intersect for $(M/D_d)_{1c} \approx 9.31854 \times 10^{-13}$. *Below middle and right*: The angular separations $\theta_{1p} - \theta_{2p}$ and $\theta_{1p} - \theta_{1s}$ among relativistic images versus M/D_d are plotted for the same values of $\mathcal{D}$ as in figures on top. θ_{2p} and θ_{1s} stand for angular positions of relativistic images of second order on the primary image side and of first order on the secondary image side, respectively. The angular source position $\beta = 1$ μas for all figures.

secondary images are too close to appear resolved on the figure. However, angular position of a primary image is always greater than that of a secondary image. The angular separation between primary and secondary images increases with increase in the value of M/D_d and $\mathcal{D}$. Further, we plot position of the first order relativistic image θ_{1p} against M/D_d for $\mathcal{D} = 0.5$, 0.05, and 0.005. (We do not plot image positions for the second order relativistic images θ_{2p}, because on chosen scales these do not appear separate from the curve for θ_{1p}.) For a fixed value of $\mathcal{D}$ and order n, θ_{np} increases with increase in M/D_d. The curves for different values of $\mathcal{D}$ are too close to appear separate on the figure. Note that there is a critical value of M/D_d at which curves for different values of $\mathcal{D}$ intersect. For the first order relativistic images on the primary image side, $(M/D_d)_{1c} \approx 9.31854 \times 10^{-13}$. For $M/D_d < (M/D_d)_{1c}$ and $M/D_d > (M/D_d)_{1c}$, the value of θ_{1p} are, respectively, lower and higher for higher value of $\mathcal{D}$. Obviously, for $M/D_d = (M/D_d)_{1c}$, θ_{1p} is the same for any value of $\mathcal{D}$. Similarly, the critical value for the second order relativistic images, $(M/D_d)_{2c} \approx 9.33022 \times 10^{-13}$ and the above results apply for θ_{2p} also. We find that $(M/D_d)_{2c} > (M/D_d)_{1c}$. For any given value of M/D_d and order n, the angular positions of relativistic images (on the secondary image side) are higher for higher $\mathcal{D}$. In the next paragraph, we show that at critical values for M/D_d, the effective deflection angles of relativistic images on the primary side are zero. The critical value of M/D_d for any given order of

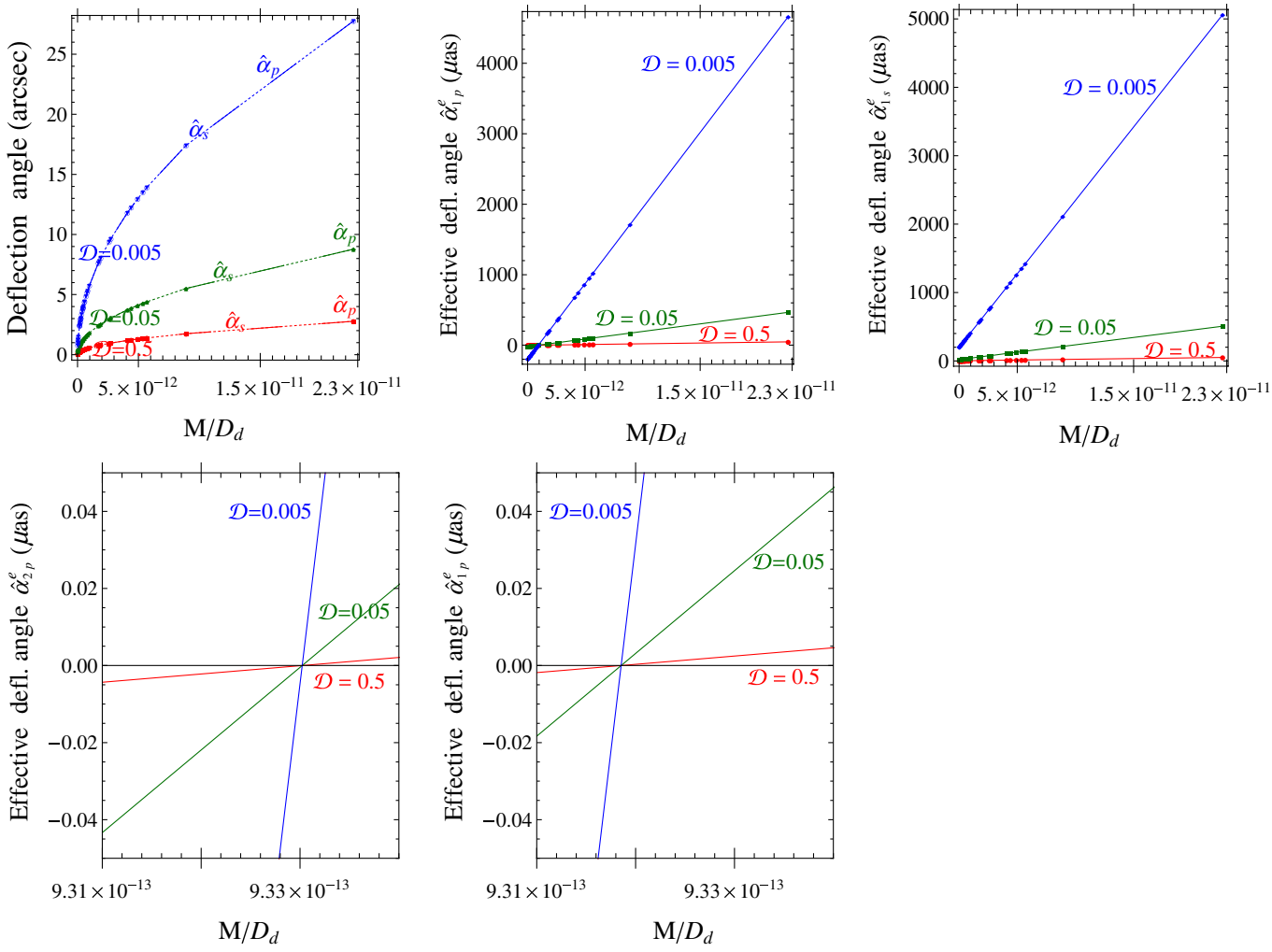

FIG. 9 (color online). *Top left*: The deflection angles of primary images $\hat{\alpha}_p$ (represented by continuous curves) and of secondary images $\hat{\alpha}_s$ (represented by dotted curves) are plotted against M/D_d of MDOs at centers of many galaxies for $\mathcal{D} = 0.5$, 0.05 and 0.005. *Top middle and right*: The effective deflection angles of relativistic images of the first order on the same side as the primary image $\hat{\alpha}^e_{1p}$ and on the secondary image side $\hat{\alpha}^e_{1s}$ are plotted against M/D_d of MDOs for the same values of $\mathcal{D}$ as in the left figure. *Below*: The effective deflection angles of relativistic images on the primary image side of the second order $\hat{\alpha}^e_{2p}$ and of the first order $\hat{\alpha}^e_{1p}$ versus M/D_d are plotted in the vicinity of zero effective deflection angle for the same values of $\mathcal{D}$. The curves for different values of $\mathcal{D}$ on left and right figures intersect, respectively, for $(M/D_d)_{2c} \approx 9.33022 \times 10^{-13}$ and $(M/D_d)_{1c} \approx 9.31854 \times 10^{-13}$. The angular source position $\beta = 1$ μas for all figures.

relativistic image depends on the value of the angular source position. We further plot angular separations between first order relativistic images (i.e., $\theta_{1p} - \theta_{1s}$) and between relativistic images (both on the primary image side) of the first and second orders (i.e., $\theta_{1p} - \theta_{2p}$) against M/D_d for $\mathcal{D} = 0.5$, 0.05, and 0.005. Our results show that variations in angular positions of relativistic images and their separations are extremely small (insignificant) due to change in the value of $\mathcal{D}$.

In Fig. 9, we first plot deflection angles for primary and secondary images against M/D_d (the ratio of mass to distance of lens) for $\mathcal{D} = 0.5$, 0.05, and 0.005. As we have taken the angular source position β a very small value, the curves for primary and secondary images do not appear separate on the figure. The deflection angles for these images increase with increase in the value of M/D_d (for a fixed value of $\mathcal{D}$) and decrease with an increase in $\mathcal{D}$ (for a fixed value of M/D_d). We now plot the effective deflection angles of the first order relativistic images on each side of the optical axis. The dependence of these effective deflection angles on $\mathcal{D}$ and M/D_d is qualitatively similar as for deflection angles for primary and secondary images. However, there is an important difference. The deflection angles of primary and secondary images, and

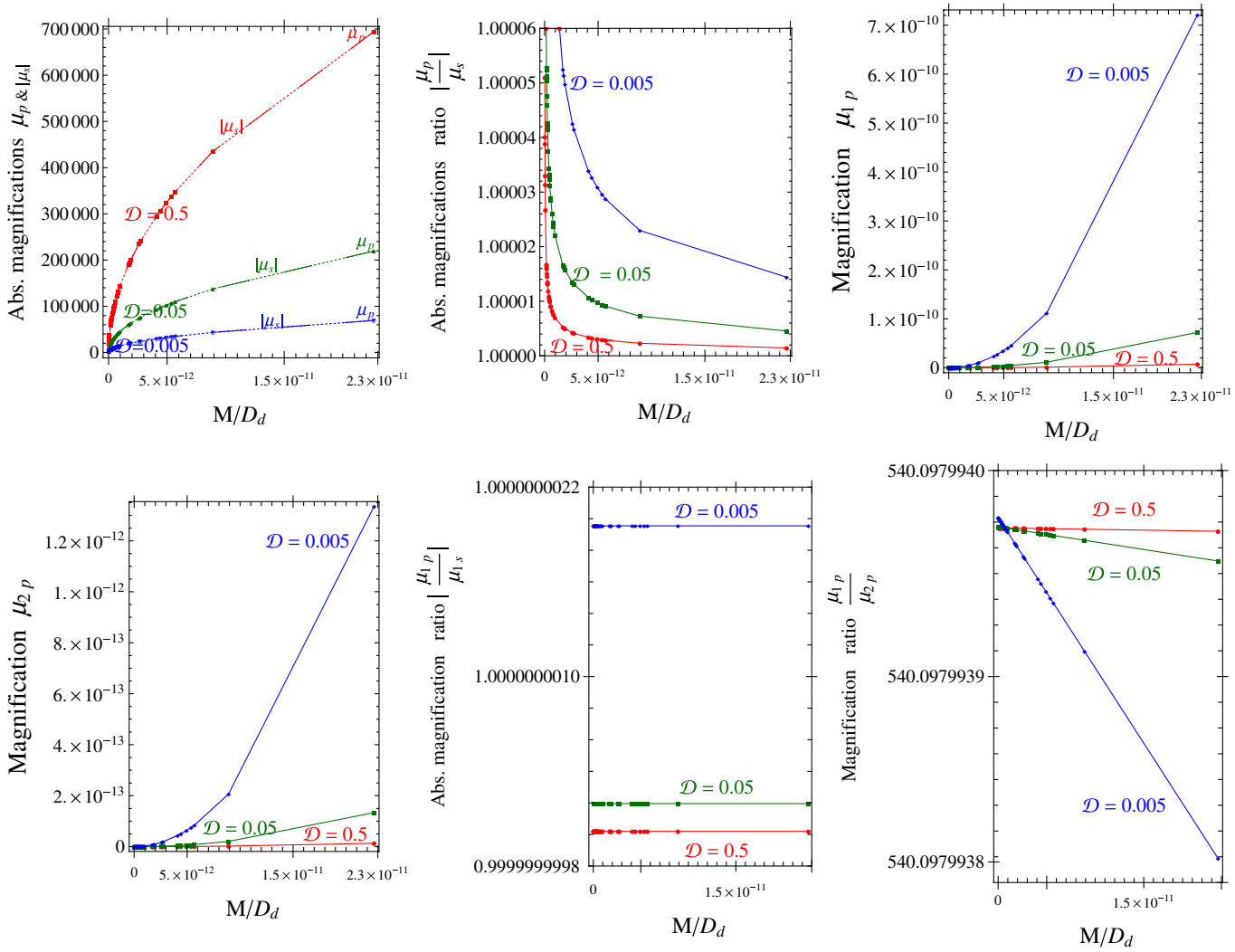

FIG. 10 (color online). *Top left and top middle*: The magnifications of primary images μ_p (represented by continuous curves) and the absolute magnifications of secondary images $|\mu_s|$ (represented by dotted curves), and their ratios $|\mu_p/\mu_s|$ vs M/D_d of MDOs at centers of many galaxies are plotted for $\mathcal{D} = 0.5$, 0.05 and 0.005. *Top right and below left*: The magnifications of relativistic images (on the same side as the primary image) of the first order μ_{1p} and of the second order μ_{2p} are plotted against M/D_d of MDOs for same values of $\mathcal{D}$. *Below middle*: The ratio of absolute magnifications of relativistic images of first order on the primary image side μ_{1p} to that on the secondary image side $|\mu_{1s}|$ are plotted against M/D_d for $\mathcal{D} = 0.5$, 0.05 and 0.005. *Below right*: The ratio of absolute magnifications of relativistic images (on the primary image side) of the first order μ_{1p} to the second order μ_{2p} are plotted against M/D_d for same values of $\mathcal{D}$ as in other plots. The curves μ_{1p}/μ_{2p} vs M/D_d for different values of $\mathcal{D}$ intersect for $M/D_d \approx 7.07130 \times 10^{-13}$. For all figures, the angular source position $\beta = 1$ μas.

effective deflection angles of relativistic images on the secondary image side are always positive. However, the effective deflection angles of relativistic images on the primary image side are negative, zero, or positive depending on the value of M/D_d. The critical value of the ratio (where the effective deflection angles are zero) for the first and second order relativistic images are $(M/D_d)_{1c} \approx 9.31854 \times 10^{-13}$ and $(M/D_d)_{2c} \approx 9.33022 \times 10^{-13}$, respectively. These values are exactly the same as we obtained for intersections of curves for image positions for different values of $\mathcal{D}$ (see the previous paragraph).

In Fig. 10, we first plot (absolute) magnifications of primary and secondary images, and their ratios against M/D_d for $\mathcal{D} = 0.5$, 0.05, and 0.005. The magnifications increase with increase in the value of M/D_d (for a fixed value of $\mathcal{D}$) as well as $\mathcal{D}$ (for a fixed value of M/D_d). As the chosen angular source position is very small, the ratio of these magnifications is very close to 1. We then plot magnifications of relativistic images of first and second orders (both on the primary image side) for $\mathcal{D} = 0.5$, 0.05, and 0.005. We also plot the ratios of (absolute) magnifications of relativistic images of order 1 on the primary image side to the secondary image side against M/D_d. We finally plot the ratio of magnifications of relativistic images of orders 1 and 2 (both on the primary image side) versus M/D_d for same values of $\mathcal{D}$. Compared to the ratios of (absolute) magnifications of primary to secondary images, the ratios of (absolute) magnifications of relativistic images are much less sensitive to changes in M/D_d and $\mathcal{D}$. The curves μ_{1p}/μ_{2p} vs M/D_d, for different values of $\mathcal{D}$, intersect for $M/D_d \approx 7.07130 \times 10^{-13}$. For M/D_d less and more than its value on the intersection point, μ_{1p}/μ_{2p} are, respectively, higher and lower for a lower value of $\mathcal{D}$. As for the case of primary and secondary images for any given value of $\mathcal{D}$, magnifications of relativistic images increase with increase in the value of M/D_d. However, there is a substantially and observationally very important difference in both cases. For a given value of M/D_d, just opposite to the case of primary and secondary images, the (absolute) magnifications of relativistic images increase with decrease in the value of $\mathcal{D}$. Therefore, sources nearer to the lens (with other conditions remaining the same) would give relativistic images of higher magnifications.

In Fig. 11, we first study the variation in the ratio of mass of lens to differential time delays among images for the change in the value of M/D_d for $\mathcal{D} = 0.5$, 0.05, and 0.005. We consider differential time delays between secondary

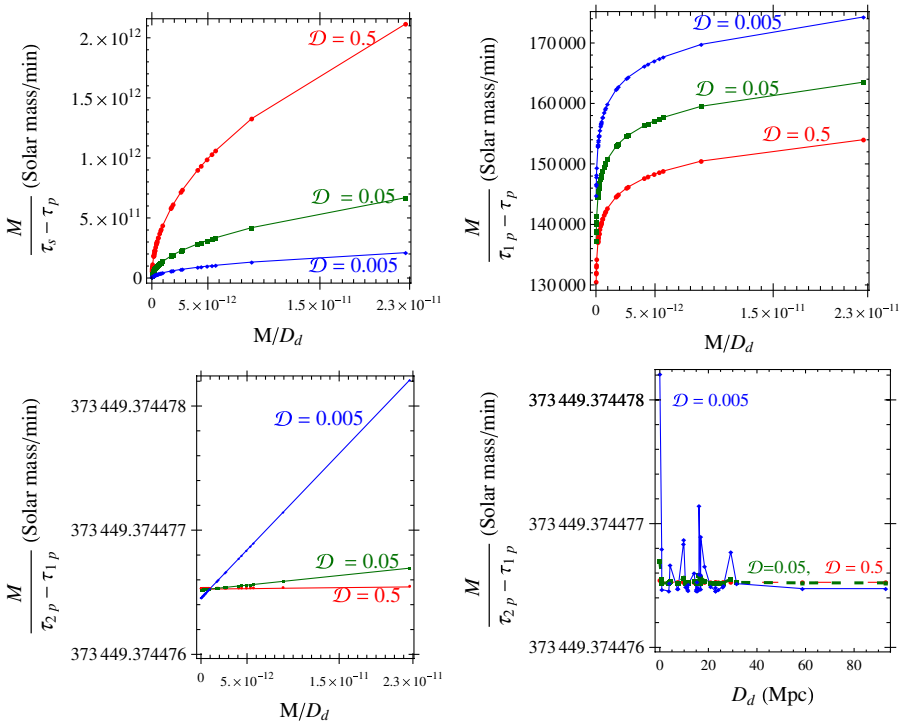

FIG. 11 (color online). *Top left, top right, and below left*: The ratios of mass M of the lens to the differential time delays of images vs M/D_d (the ratio of the mass of the lens to its distance) are plotted for $\mathcal{D} = 0.5$, 0.05 and 0.005. τ_p and τ_s stand, respectively, for time delays of primary and secondary images, whereas τ_{1p} and τ_{2p}, respectively, represent time delays of relativistic images (on the same side as the primary image) of orders 1 and 2. The curves on below left plot intersect for $M/D_d \approx 9.32438 \times 10^{-13}$. For a given value of $\mathcal{D}$, ratios of mass to differential time delay are strictly increasing function of M/D_d. *Below right*: The ratios of mass M of the lens to the differential time delay $(\tau_{2p} - \tau_{1p})$ of images are plotted against the distance D_d of the lens for same values of $\mathcal{D}$. The ratio $M/(\tau_{2p} - \tau_{1p})$ is not a function of D_d. The angular source position $\beta = 1$ μas for all figures.

and primary images ($\tau_s - \tau_p$), the first order relativistic image on the primary image side and the primary image ($\tau_{1p} - \tau_p$), and second order and first order relativistic images both on the primary image side ($\tau_{2p} - \tau_{1p}$). We take the angular source position $\beta = 1$ μas. The ratio $M/(\tau_s - \tau_p)$ increases with an increase in M/D_d (for a fixed value of $\mathcal{D}$) as well as an increase in $\mathcal{D}$ (for a fixed value of M/D_d). It is obvious from the figure that this ratio is very sensitive to changes in distances involved in GL. The ratio $M/(\tau_{1p} - \tau_p)$ increases with increase in M/D_d (for a fixed value of $\mathcal{D}$); however, it decreases with increase in $\mathcal{D}$ (for a fixed value of M/D_d). This ratio is less (compared to the first we discussed) sensitive to changes in M/D_d and $\mathcal{D}$. The third ratio $M/(\tau_{2p} - \tau_{1p})$ also increases with an increase in M/D_d (for a fixed value of $\mathcal{D}$); however, for a fixed M/D_d, the variation against $\mathcal{D}$ is more fascinating. There exists a critical value of $M/D_d \approx 9.32438 \times 10^{-13}$ for which curves for different values of $\mathcal{D}$ intersect. For M/D_d less and more than this critical value, the ratio $M/(\tau_{2p} - \tau_{1p})$ is, respectively, less and more for smaller value of $\mathcal{D}$. This ratio is extremely insensitive to changes in $\mathcal{D}$ and M/D_d, and also in β (as shown in Sec. V). Therefore, this ratio can be considered almost a constant and can be used to estimate very accurate values for masses of lenses once the differential time delays $\tau_{2p} - \tau_{1p}$ are known. We also compute this ratio for all MDOs (listed on Table IV) for a few values of $\mathcal{D} > 0.5$ (these results are not shown on the plot). We find that the slope at any point on $M/(\tau_{2p} - \tau_{1p})$ vs M/D_d curve tends to 0 as $\mathcal{D} \to 1$. We finally plot $M/(\tau_{2p} - \tau_{1p})$ against D_d for different values of $\mathcal{D}$. We find that the ratio $M/(\tau_{2p} - \tau_{1p})$ is extremely insensitive to changes in $\mathcal{D}$ as well as D_d. Fluctuation in the value of this ratio decreases with increase in $\mathcal{D}$. For a fixed value of $\mathcal{D}$, we find that the ratio $M/(\tau_{2p} - \tau_{1p})$ has more than 1 value for the same value of D_d; therefore, this ratio is not a function of D_d. However, note that, for any fixed value of $\mathcal{D}$, ratios of mass of the lens to the differential time delay are strictly increasing functions of M/D_d.

Comparison with Bozza and Mancini's results

Bozza and Mancini (BM) [18] obtained differential time delays among relativistic images due to GL by a general static spherically symmetric spacetime. They further modeled MDOs of 12 galaxies as Schwarzschild lenses, considered $\mathcal{D} = 0.5$ (i.e., the lenses to be symmetrically situated between sources and observers) and the angular source position $\beta = 0$. Using their analytical expression for differential time delays among relativistic images, they computed differential time delays between relativistic images of orders 1 and 2; i.e., $(\tau_2 - \tau_1)$, where τ_1 and τ_2 are, respectively, time delays of relativistic images of orders 1 and 2 for $\beta = 0$. We put their results in Table VII in decreasing order of M/D_d of lenses. We now consider the same set of MDOs and use the same values for mass M and distance D_d used in their paper. We do not use the updated values for M and D_d in this subsection, because we want to compare BM's results with ours. Our approach is numerical and we do not take either weak or strong field approximation. As considered by those authors, we also take $\mathcal{D} = 0.5$ and $\beta = 0$, and compute differential time delays of relativistic images of orders 1 and 2. We then compute percentage difference $= 100(x - y)/x$ between ours and their results, where x and y are, respectively, differential time delays obtained by us and BM. We find that the percentage difference ranges approximately from

TABLE VII. Comparison of Bozza and Mancini's approximate analytical [18] and our numerical results. Mass and distance of MDOs are given in the units of *solar mass* and *Mpc*, respectively. M/D_d in the third column is dimensionless ($M \equiv MG/c^2$). Differential time delays $\tau_2 - \tau_1$ are expressed in *minutes*. τ_2 and τ_1 stand, respectively, for time delays of the first and second order relativistic images for the angular source position $\beta = 0$. The ratio of source-lens to source-observer distances $\mathcal{D} = 0.5$. The ratio of mass of an MDO to the differential time delay $M/(\tau_2 - \tau_1)$ is expressed in terms of *solar mass/minute*. Masses and distances of MDOs in this table are taken the same as in [18].

MDO in galaxy	Mass M	Distance D_d	M/D_d	Differential time delay $(\tau_2 - \tau_1)$			$M/(\tau_2 - \tau_1)$	
				Analytical	Numerical	%difference	Analytical	Numerical
Milky Way	2.8×10^6	0.0085	1.57×10^{-11}	6	7.4977	20.0	466666.666666667	373449.374476538
NGC3115	2.0×10^9	8.4	1.14×10^{-11}	5430	5355.5	−1.4	368324.125230203	373449.374476535
NGC4486(M87)	3.3×10^9	15.3	1.03×10^{-11}	8958	8836.5	−1.4	368385.800401875	373449.374476534
NGC4594	1.0×10^9	9.2	5.20×10^{-12}	2712	2677.7	−1.3	368731.563421829	373449.374476530
NGC4374(M84)	1.4×10^9	15.3	4.37×10^{-12}	3798	3748.8	−1.3	368615.060558189	373449.374476529
NGC224(M31)	3.0×10^7	0.7	2.05×10^{-12}	84	80.332	−4.6	357142.857142857	373449.374476527
NGC4486B(M104)	5.7×10^8	15.3	1.78×10^{-12}	1548	1526.3	−1.4	368217.054263566	373449.374476527
NGC4342(IC3256)	3.0×10^8	15.3	9.37×10^{-13}	816	803.32	−1.6	367647.058823529	373449.374476527
NGC3377	1.8×10^8	9.9	8.69×10^{-13}	486	481.99	−0.8	370370.370370370	373449.374476527
NGC4261	4.5×10^8	27.4	7.85×10^{-13}	1224	1205.0	−1.6	367647.058823529	373449.374476526
NGC7052	3.3×10^8	58.7	2.69×10^{-13}	894	883.65	−1.2	369127.516778523	373449.374476526
NGC0221(M32)f	3.4×10^6	0.7	2.32×10^{-13}	12	9.1043	−31.8	283333.333333333	373449.374476526

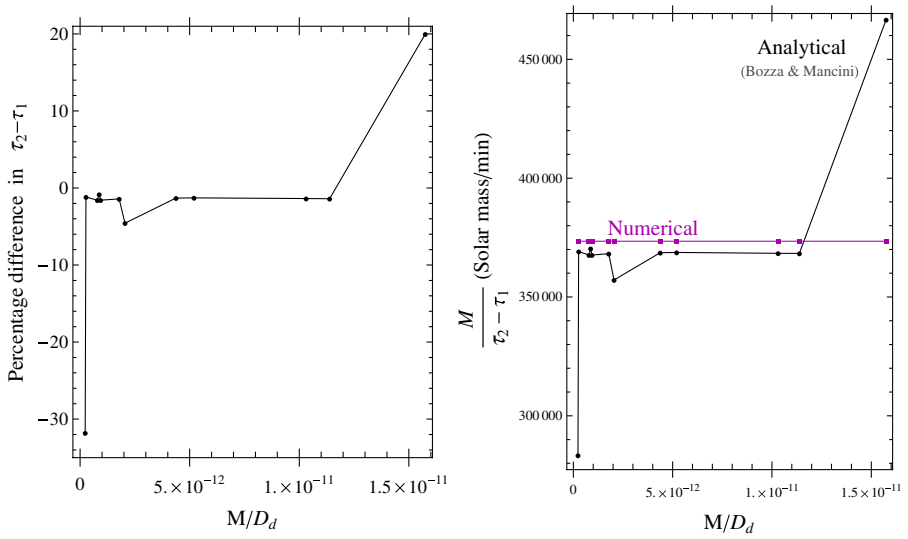

FIG. 12 (color online). *Left*: The percentage difference in values for differential time delays $(\tau_2 - \tau_1)$ obtained by Bozza and Mancini [18] (using analytical method) and by us (using numerical method) is plotted against M/D_d of MDOs at centers of a few galaxies. τ_1 and τ_2, respectively, stand for time delays of relativistic images of orders 1 and 2. *Right*: The ratios of mass M of the lens to the differential time delay $(\tau_2 - \tau_1)$ vs M/D_d are plotted for both cases. Our numerical results show that the ratio $M/(\tau_2 - \tau_1)$ is strictly increasing function of M/D_d. Masses and distances of MDOs are taken from [18] and are given in Table VII. $\mathcal{D} = 0.5$ and the angular source position $\beta = 0$ in both figures.

-31.8% to 20.0%, which are large. It is possible that MDOs of other galaxies (i.e., excluding those considered by BM) give even higher percentage differences. We plot the percentage difference in these results against M/D_d (see Fig. 12). Further, using BM as well as our results, we compute $M/(\tau_2 - \tau_1)$ for MDOs. We give these results in Table VII. We then plot this ratio against M/D_d (see Fig. 12). Results obtained by BM show that the ratio $M/(\tau_2 - \tau_1)$ fluctuates quite irregularly (showing no rhythm) with an increase in the value of M/D_d for otherwise constant situation. There seems to be no physical argument in support for this. On the other hand, our results show that $M/(\tau_2 - \tau_1)$ is a strictly increasing (though the increase rate is extremely small) function of M/D_d. As we did not take either weak or strong field approximation at any stage of computation and performed numerical computation with high precision, our results are very accurate. Therefore, we consider percentage differences in results as percentage errors in their results.

VI. DISCUSSION AND SUMMARY

It is well-known that the observation of primary and secondary images due to GL by an MDO at the center of a galaxy is very difficult due to a large extinction of electromagnetic radiation (larger extinction for smaller wavelength) in the vicinity of a galactic center. In addition, radiations at several wavelengths from materials accreting on an MDO badly hinders observation of these images. These obstacles would be even bigger for relativistic images as, compared to primary and secondary images, these are formed much closer to the center of a galaxy. Unfortunately, observations of relativistic images would be much more difficult due to some additional reasons. Relativistic images are very much demagnified, unless the lens components (the source, the lens, and the observer) are perfectly or highly aligned ($\beta \ll 1$ μas), and therefore these images are extremely difficult to be observed. Supernovae could be more suitable sources for observation of relativistic images, but the probability that a supernova will be highly aligned with the lens and observer is extremely small. However, there is a silver lining to the demagnification problem associated with observation of relativistic images: magnifications of relativistic images increase rapidly with the decrease in the value of $\mathcal{D}$; i.e., with the decrease in the source-lens distance for otherwise constant situation. Thus, sources closer to a galactic center would give less demagnified relativistic images. Despite this, there is no doubt that the observation of relativistic images would be a Herculean task. However, with improved observational facilities in future and through lucky observations (due to a bright source close to a galactic center and highly aligned with the galactic center and the observer), the relativistic images could possibly be detected some day. Today's these almost unthinkable events may be tomorrow's observations. The detection of relativistic images would be definitely one of the most important discovery in astronomy and would have immense implications for general relativity and relativistic astrophysics. For examples, these observations would provide a test for the general theory of relativity in a strong gravitational field. In [9], we discussed that observation of relativistic images would give upper bound to the compactness of MDOs and therefore would strongly support that these MDOs are

black holes. The measurements of physical quantities for relativistic images would also give very accurate values for masses and distances of black holes.

For any fixed value of $\mathcal{D}$, the ratio of mass M of a Schwarzschild lens to differential time delay $(\tau_{2p} - \tau_{1p})$ or $(\tau_{2s} - \tau_{1s})$ is not a function of the lens-observer distance D_d; however, it is a strictly increasing function of M/Dd. Computations show that the ratio $M/(\tau_{2p} - \tau_{1p})$ is *extremely* insensitive to changes in the angular source position as well as the observer-lens and lens-source distances, and therefore this awesome physical quantity must be treasured as an almost constant for purpose of measurements. Thus, once we succeed in detecting relativistic images and measuring the differential time delay, we can immediately compute a very accurate value of mass of the MDO acting as a lens. (The accuracy of the result for the mass of the MDO will however depend on the accuracy of the measurement of differential time delay.) Our computations show that for $M/D_d = (0, 2.265 \times 10^{-11})$ and $\mathcal{D} = [0.005, 1)$,

$$M \approx 3.734493744773 \times 10^5 (\tau_{2p} - \tau_{1p}), \qquad (19)$$

where mass M of the MDO and the differential time delay $\tau_{2p} - \tau_{1p}$ are expressed in units of *solar mass* and *minute*, respectively. As relativistic images can possibly be observed when the lens components are perfectly or highly aligned, we took the angular source position $\beta = 1$ μas for computations. However, we found extremely small changes in results for computations with $\beta = 0$. Once, the value of mass of the MDO is known, its distance can be computed from the results given in Fig. 8 (below). Angular separations between relativistic images depend on the ratio M/D_d, but fortunately it is extremely insensitive to the change in the value of $\mathcal{D}$. This would help us measure the distance of the MDO very accurately once we have the mass of the MDO and the angular separation between relativistic images is measured. It is worth mentioning that accuracies in determination of distances of black holes would, however, depend on accuracies of our measurements of differential time delays and angular separations between relativistic images. The dependence of (absolute) magnifications ratio of relativistic images of the first order (i.e., $|\mu_{1p}/\mu_{1s}|$) on M/D_d is extremely small (see Fig. 10). Therefore, measurement of the magnifications ratio would give very accurate value for $\mathcal{D}$. This result with already obtained value for observer-lens distance D_d would give observer-source distance D_s. In Sec. V, we discussed that results of Bozza and Mancini [18] show that the ratio $M/(\tau_2 - \tau_1)$ fluctuates quite irregularly with an increase in the value of M/D_d and their results have large errors. In [28], they expressed this ratio as a constant; however, that also yields result with considerable error.

Effective deflection angles of relativistic images play a very significant role in analyzing and understanding these images. The deflection angles for primary-secondary image pair as well as relativistic images of Schwarzschild black hole lensing are always positive. The effective deflection angles of relativistic images of any order on the secondary image side are also always positive. However, the effective deflection angles of relativistic images of any order on the primary image side may be positive, zero, or negative depending on the value of the angular source position β and the ratio of mass of the lens to its distance (i.e., M/D_d). For a relativistic image (on the primary image side) of any order n and for any value of M/D_d of the lens, there exists a critical angular source position β_{nc} such that the effective deflection angle $\hat{\alpha}^e_{np}$ for that relativistic image is zero. For $\beta < \beta_{nc}$, $\hat{\alpha}^e_{np} > 0$, and for $\beta > \beta_{nc}$, $\hat{\alpha}^e_{np} < 0$. For a given value of M/D_d, β_{nc} is smaller for smaller n. All sources at $\beta = \beta_{nc}$ are lensed to give rise to n^{th} order relativistic images (on primary image side) at the same angular position $\theta_{np} = \beta_{nc}$. For a fixed value of M/D_d, the angular positions of relativistic images are extremely insensitive to changes in the angular source position as well as the lens-source distance. However, for a theoretical interest, it is worth noting that for $\beta < \beta_{nc}$ and $\beta > \beta_{nc}$, the value of θ_{np} is, respectively, higher and lower for higher value of $\mathcal{D}$. The critical angular source position plays a role of flipping point for image positions with respect to the change in the value of $\mathcal{D}$. These results help us conclude the following: For different sources at the same angular position, relativistic images with positive, zero, and negative effective deflection angles have, respectively, bigger, equal, and smaller (absolute) angular positions for bigger values of $\mathcal{D}$. This is also true for primary and secondary images, as deflection angles for them are always positive. These conclusions can be also derived from the lens equation. Therefore, these results support correctness of our numerical computations.

In GL observations, differential time delays among images (not the time delays of individual images) have been measured until now. For this reason, studies of time delays of images have not drawn enough attention. The most well-known book on GL gives an expression for time delays of gravitationally lensed images [see Eq. (4.67) in [3]]. The equation has an additive constant term. The authors clearly stated that the constant term is the same for all rays from the observer to the source plane. Though the value for the constant term is not yet determined, the expression given in the book is good enough to compute differential time delays among images. This is because the constant term cancels for images of the same source by the same lens. It is of theoretical interest to study time delays of gravitationally lensed images. It might also be possible in future to develop a method to measure time delays of images. These motivated us to first compute time delays of images and then use these results to compute differential time delays among them. As Eq. (4.67) in [3] cannot be used to compute time delays of images, we used the method given

in Weinberg's book. Our results for time delays of primary and secondary images turn out to be counterintuitive and very fascinating (see Fig. 6). For instance, time delays of primary images are always smaller for sources nearer to the lens for otherwise constant situation. Time delays results for relativistic images are also very interesting and important.

GL as well as gravitational retro-lensing give rise to very much demagnified images due to light deflections in strong gravitational field. Images due to these two phenomena can be observationally easily differentiated by the fact that the images due to the latter are ''orphans'' in a sense that these are not accompanied by primary-secondary images pair as their ''parents''. In this paper, we have studied only images due to GL. Eiroa and Torres [29] studied retro-lensing by a Schwarzschild black hole. They compared magnifications of gravitationally retro-lensed images and relativistic images of GL of the same order (i.e., the number of turns a light ray makes around the lens before reaching the observer) and found that the former is significantly greater than the latter. Black holes have angular momentum. Therefore, Cunninghom and Bardeen [30] and Rauch and Blandford [31] pioneered Kerr black hole lensing. As there has been mounting observational evidence in support of existence of black holes, Kerr lensing has become a very lively research topic (see [32] and references therein) these days. It is worth investigating the behavior of the ratio of mass M of the lens to differential time delays of images of strong field lensing due to changes in β, M/D_d, $\mathcal{D}$, and a/M (a is the rotational parameter of the Kerr metric). These investigations are likely to have immense implication for relativistic astrophysics.

With increasing observational support for MDOs at centers of galaxies and stellar size black hole candidates to be black holes, the pressure to believe in the existence of black holes in the Universe has began to mount. However, by the definition of a black hole, there cannot be an iron-clad observational evidence that a black hole candidate is indeed a black hole. Given that the *weak cosmic censorship hypothesis* (WCCH) of Penrose is still unproven (see [33] and references therein), there is no compelling scientific reason to accept that all black hole candidates are black holes and none of them can be interpreted as a *naked (visible) singularity.* Despite the fact that the concept of naked singularity does not ''smell right'' to majority of researchers, it may not be wise to completely ignore the possibility of existence of naked singularities. Researchers think that in the vicinity of a spacetime singularity, a mysterious violent marriage of general relativity and quantum physics is solemnized and opportunities to observe these (through outgoing geodesics from there to us) could help us obtain an unanimously acceptable viable quantum gravity theory. Philosophically, it is not clear to us why the nature should be malicious to always hide such awesome holy marriages from us. Inspired by these ideas, we initiated a new theoretical research project using GL phenomena that investigates whether or not black holes and naked singularities could be observationally differentiated (see [19–21]). Our computations yielded encouraging distinctive results. Whether or not the weak cosmic censorship hypothesis of Penrose finally turns out to be true, there has to be a cosmic censorship which forbids arbitrary large values of *those* nakedness parameters [e.g., $(Q/M)^2$ in the Reissner-Nordström solution to the Einstein-Maxwell equations, where Q and M stand for electric charge and mass parameters, respectively] which make the system unphysical. Motivated by this idea, we hypothesize a new cosmic censorship: Generically, marginally and strongly naked singularities do not occur in a realistic gravitational collapse. (For definitions of weakly naked, marginally naked, and strongly naked singularities, see [21]). The new cosmic censorship hypothesis (CCH) allows the existence of weakly naked singularities, but does not say that these do exist. This hypothesis does not imply that the well-known weak cosmic censorship hypothesis is incorrect. Rather, it says that in case the WCCH of Penrose turns out to be incorrect, the new cosmic censorship will hold good. In [34], we showed that a Vaidya naked singularity is weakly naked and therefore it is not a counter-example to the new CCH. The proof of the pudding is in the eating. It may be of an astrophysical interest to investigate this subject further. We will discuss the new CCH in detail in [35].

ACKNOWLEDGMENTS

Thanks are due to J. M. Aguirregabiria, H. M. Antia, M. Bartelmann, and D. Narasimha for helpful correspondence related to verification of some results of Fig. 6 (top left). Thanks are also due to F. Eisenhauer for giving me the Ref. [27] and to P. R. Anderson for a careful reading of the manuscript.

[1] In gravitational lensing theory, *weak* and *strong* fields usually refer to the regions of spacetime which cause, respectively, small and large deflections of light.
[2] A. Eddington, *Space, Time and Gravitation* (Cambridge Univ. Press, Cambridge, 1920).
[3] P. Schneider, J. Ehlers, and E. E. Falco, *Gravitational Lenses* (Springer-Verlag, Berlin, 1992).
[4] P. Schneider, C. Kochanek, and J. Wambsganss, *Gravitational Lensing: Strong, Weak and Micro* (Springer-Verlag, Berlin, 2006).

[5] R. Narayan and M. Bartelmann, arXiv:astro-ph/9606001; O. Wucknitz, arXiv:0709.4005.

[6] C. Darwin, Proc. R. Soc. A **249**, 180 (1959); **263**, 39 (1961).

[7] R. Atkinson, Astron. J. **70**, 517 (1965).

[8] S. Frittelli and E. T. Newman, Phys. Rev. D **59**, 124001 (1999).

[9] K. S. Virbhadra and G. F. R. Ellis, Phys. Rev. D **62**, 084003 (2000).

[10] S. Frittelli, T. P. Kling, and E. T. Newman, Phys. Rev. D **61**, 064021 (2000); T. P. Kling, E. T. Newman, and A. Perez, *ibid.* **62**, 024025 (2000); **62**, 109901(E) (2000).

[11] V. Perlick, arXiv:0708.0178.

[12] V. Perlick, Living Rev. Relativity **7**, 9 (2004); Phys. Rev. D **69**, 064017 (2004); Commun. Math. Phys. **220**, 403 (2001); W. Hasse and V. Perlick, J. Math. Phys. (N.Y.) **47**, 042503 (2006); Gen. Relativ. Gravit. **34**, 415 (2002); T. Foertsch, W. Hasse, and V. Perlick, Classical Quantum Gravity **20**, 4635 (2003).

[13] P. Amore, M. Cervantes, A. De Pace, and F. M. Fernandez, Phys. Rev. D **75**, 083005 (2007); P. Amore and S. Arceo, *ibid.* **73**, 083004 (2006); P. Amore, S. Arceo, and F. M. Fernandez, *ibid.* **74**, 083004 (2006).

[14] A. F. Zakharov, F. De Paolis, G. Ingrosso, and A. A. Nucita, Astron. Astrophys. **442**, 795 (2005); A. F. Zakharov, A. A. Nucita, F. De Paolis, and G. Ingrosso, New Astron. **10**, 479 (2005); A. F. Zakharov and Yu. V. Baryshev, Int. J. Mod. Phys. D **11**, 1067 (2002); Classical Quantum Gravity **19**, 1361 (2002).

[15] G. N. Gyulchev and S. S. Yazadjiev, Phys. Rev. D **75**, 023006 (2007); R. Whisker, *ibid.* **71**, 064004 (2005); C. R. Keeton and A. O. Petters, *ibid.* **73**, 044024 (2006); **73**, 104032 (2006); E. F. Eiroa, G. E. Romero, and D. F. Torres, *ibid.* **66**, 024010 (2002); E. F. Eiroa, *ibid.* **73**, 043002 (2006); A. O. Petters, Mon. Not. R. Astron. Soc. **338**, 457 (2003); S. V. Iyer and A. O. Petters, Gen. Relativ. Gravit. **39**, 1563 (2007); N. Mukherjee and A. S. Majumdar, *ibid.* **39**, 583 (2007); A. S. Majumdar and N. Mukherjee, Mod. Phys. Lett. A **20**, 2487 (2005); E. F. Eiroa, Braz. J. Phys. **35**, 1113 (2005); E. F. Eiroa and G. E. Romero, Phys. Lett. B **663**, 377 (2008); G. S. Bisnovatyi-Kogan and O. Yu. Tsupko, Astrophysics (Engl. Transl.) **51**, 99 (2008).

[16] S. Fernando and S. Roberts, Gen. Relativ. Gravit. **34**, 1221 (2002); P. Mutka and P. Mahonen, Astrophys. J. **581**, 1328 (2002); C. Stornaiolo, Gen. Relativ. Gravit. **34**, 2089 (2002); P. Mutka and P. Mahonen, Astrophys. J. **581**, 1328 (2002); K. Lake, Phys. Rev. D **65**, 087301 (2002); A. Bhadra, Phys. Rev. D **67**, 103009 (2003); R. A. Konoplya, Phys. Lett. B **644**, 219 (2007); J. Briet and D. Hobill, arXiv:0801.3859.

[17] V. Bozza, S. Capozziello, G. Iovane, and G. Scarpetta, Gen. Relativ. Gravit. **33**, 1535 (2001).

[18] V. Bozza and L. Mancini, Gen. Relativ. Gravit. **36**, 435 (2004).

[19] K. S. Virbhadra, D. Narasimha, and S. M. Chitre, Astron. Astrophys. **337**, 1 (1998).

[20] K. S. Virbhadra and G. F. R. Ellis, Phys. Rev. D **65**, 103004 (2002).

[21] K. S. Virbhadra and C. R. Keeton, Phys. Rev. D **77**, 124014 (2008); See also arXiv:0710.2333V1 for more results in tables.

[22] G. N. Gyulchev and S. S. Yazadjiev, Phys. Rev. D **78**, 083004 (2008); M. C. Werner and A. O. Petters, *ibid.* **76**, 064024 (2007).

[23] M. Safonova and D. F. Torres, Mod. Phys. Lett. A **17**, 1685 (2002); J. M. Tejeiro and E. A. Larranaga, arXiv:gr-qc/0505054; K. K. Nandi, Phys. Rev. D **74**, 024020 (2006); F. Rahaman, M. Kalam, and S. Chakraborty, Chin. J. Phys. (Taipei) **45**, 518 (2007); T. K. Dey and S. Sen, Mod. Phys. Lett. A **23**, 953 (2008).

[24] V. Kagramanova, J. Kunz, and C. Lämmerzahl, Phys. Lett. B **634**, 465 (2006); I. Ciufolini and F. Ricci, Classical Quantum Gravity **19**, 3863 (2002); **19**, 3875 (2002); S. S. Yazadjiev, arXiv:gr-qc/0305053; M. P. Dabrowski and F. E. Schunck, Astrophys. J. **535**, 316 (2000); T. Matos and R. Becerril, Classical Quantum Gravity **18**, 2015 (2001); V. A. De Lorenci, N. Figueiredo, H. H. Fliche, and M. Novello, Astron. Astrophys. **369**, 690 (2001); F. E. Schunck, B. Fuchs, and E. W. Mielke, Mon. Not. R. Astron. Soc. **369**, 485 (2006); K. Sarkar and A. Bhadra, Classical Quantum Gravity **23**, 6101 (2006); Y. Chen, Z. Chen, and J. Wang, Gen. Relativ. Gravit. **39**, 401 (2007); B. Gwak, B-H. Lee, and W. Lee, arXiv:0806.4320.

[25] S. Weinberg, *Gravitation and Cosmology: Principles and Applications of the General Theory of Relativity* (Wiley, New York, 1972).

[26] F. Eisenhauer *et al.*, Astrophys. J. **628**, 246 (2005).

[27] K. Gebhardt, http://hoku.as.utexas.edu/~gebhardt/blackhole.html.

[28] V. Bozza and L. Mancini, Astrophys. J. **611**, 1045 (2004).

[29] E. F. Eiroa and D. F. Torres, Phys. Rev. D **69**, 063004 (2004).

[30] C. T. Cunningham and J. M. Bardeen, Astrophys. J. **183**, 237 (1973).

[31] K. P. Rauch and R. D. Blandford, Astrophys. J. **421**, 46 (1994).

[32] S. E. Vazquez and E. P. Esteban, Nuovo Cimento B **119**, 489 (2004).

[33] R. Penrose, in *Black Holes and Relativistic Stars*, edited by R. M. Wald (The University of Chicago , Chicago, 1998), p. 103; K. S. Virbhadra, S. Jhingan, and P. S. Joshi, Int. J. Mod. Phys. D **6**, 357 (1997); K. S. Virbhadra, Int. J. Mod. Phys. A **12**, 4831 (1997); Phys. Rev. D **60**, 104041 (1999).

[34] C-M. Claudel, K. S. Virbhadra, and G. F. R. Ellis, J. Math. Phys. (N.Y.) **42**, 818 (2001).

[35] K. S. Virbhadra, Gravitational lensing by Reissner-Nordström black holes and naked singularities (unpublished).